



SERENADE. II. An ALMA Multiband Dust Continuum Analysis of 28 Galaxies at $5 < z < 8$ and the Physical Origin of the Dust Temperature

Downloaded from: <https://research.chalmers.se>, 2024-09-11 06:23 UTC




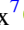





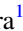
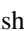

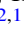

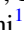


Citation for the original published paper (version of record):

Mitsuhashi, I., Harikane, Y., Bauer, F. et al (2024). SERENADE. II. An ALMA Multiband Dust Continuum Analysis of 28 Galaxies at $5 < z < 8$ and the Physical Origin of the Dust Temperature Evolution. *Astrophysical Journal*, 971(2).
<http://dx.doi.org/10.3847/1538-4357/ad5675>

N.B. When citing this work, cite the original published paper.



SERENADE. II. An ALMA Multiband Dust Continuum Analysis of 28 Galaxies at $5 < z < 8$ and the Physical Origin of the Dust Temperature Evolution

Ikki Mitsuhashi^{1,2,11} , Yuichi Harikane³ , Franz E. Bauer^{4,5,6} , Tom J. L. C. Bakx⁷ , Andrea Ferrara⁸ , Seiji Fujimoto⁹ , Takuya Hashimoto¹⁰ , Akio K. Inoue^{11,12} , Kazushi Iwasawa^{13,14} , Yuri Nishimura¹ , Masatoshi Imanishi² , Yoshiaki Ono³ , Toshiki Saito², Yuma Sugahara^{2,11} , Hideki Umehata^{15,16,17} , Livia Vallini¹⁸ , Tao Wang^{19,20} , and Jorge A. Zavala² 

¹ Department of Astronomy, The University of Tokyo, 7-3-1 Hongo, Bunkyo, Tokyo 113-0033, Japan; ikki0913astr@gmail.com

² National Astronomical Observatory of Japan, 2-21-1 Osawa, Mitaka, Tokyo 181-8588, Japan

³ Institute for Cosmic Ray Research, The University of Tokyo, 5-1-5 Kashiwanoha, Kashiwa, Chiba 277-8582, Japan

⁴ Instituto de Astrofísica and Centro de Astroingeniería, Facultad de Física, Pontificia Universidad Católica de Chile, Campus San Joaquín, Av. Vicuña Mackenna 4860, Macul Santiago, 7820436, Chile

⁵ Millennium Institute of Astrophysics, Nuncio Monseñor Sótero Sanz 100, Of 104, Providencia, Santiago, Chile

⁶ Space Science Institute, 4750 Walnut Street, Suite 205, Boulder, CO 80301, USA

⁷ Department of Space, Earth and Environment, Chalmers University of Technology, Gothenburg, Sweden

⁸ Scuola Normale Superiore, Piazza dei Cavalieri 7, I-56126, Pisa, Italy

⁹ Department of Astronomy, The University of Texas at Austin, 2515 Speedway Boulevard Stop C1400, Austin, TX 78712-1205, USA

¹⁰ Tomonaga Center for the History of the Universe (TCHoU), Faculty of Pure and Applied Sciences, University of Tsukuba, Tsukuba, Ibaraki 305-8571, Japan

¹¹ Waseda Research Institute for Science and Engineering, Faculty of Science and Engineering, Waseda University, 3-4-1, Okubo, Shinjuku, Tokyo 169-8555, Japan

¹² Department of Physics, School of Advanced Science and Engineering, Faculty of Science and Engineering, Waseda University, 3-4-1, Okubo, Shinjuku, Tokyo 169-8555, Japan

¹³ Institut de Ciències del Cosmos (ICCUB), Universitat de Barcelona (IEEC-UB), Martí i Franquès, 1, 08028 Barcelona, Spain

¹⁴ ICREA, Pg. Lluís Companys 23, 08010 Barcelona, Spain

¹⁵ Institute for Advanced Research, Nagoya University, Furocho, Chikusa, Nagoya 464-8602, Japan

¹⁶ Department of Physics, Graduate School of Science, Nagoya University, Furocho, Chikusa, Nagoya 464-8602, Japan

¹⁷ Cahill Center for Astronomy and Astrophysics, California Institute of Technology, MS 249-17, Pasadena, CA 91125, USA

¹⁸ INAF-Osservatorio di Astrofisica e Scienza dello Spazio, via Gobetti 93/3, I-40129, Bologna, Italy

¹⁹ School of Astronomy and Space Science, Nanjing University, Nanjing, Jiangsu 210093, People's Republic of China

²⁰ Key Laboratory of Modern Astronomy and Astrophysics, Nanjing University, Ministry of Education, Nanjing 210093, People's Republic of China

Received 2023 November 28; revised 2024 April 26; accepted 2024 May 14; published 2024 August 14

Abstract

We present an analysis of the Atacama Large Millimeter-submillimeter Array (ALMA) multiband dust continuum observations for 28 spectroscopically confirmed bright Lyman break galaxies at $5 < z < 8$. Our sample consists of 11 galaxies at $z \sim 6$ newly observed in our ALMA program, which substantially increases the number of $5 < z < 8$ galaxies with both rest-frame 88 and 158 μm continuum observations, allowing us to simultaneously measure the IR luminosity and dust temperature for a statistical sample of $z \gtrsim 5$ galaxies for the first time. We derive the relationship between the ultraviolet (UV) slope (β_{UV}) and infrared excess (IRX) for the $z \sim 6$ galaxies, and find a shallower IRX- β_{UV} relation compared to the previous results at $z \sim 2-4$. Based on the IRX- β_{UV} relation consistent with our results and the $\beta_{\text{UV}}-M_{\text{UV}}$ relation including fainter galaxies in the literature, we find a limited contribution of the dust-obscured star formation to the total star formation rate density, $\sim 30\%$ at $z \sim 6$. Our measurements of the dust temperature at $z \sim 6-7$, $T_{\text{dust}} = 40.9^{+10.0}_{-9.1}$ K on average, support a gentle increase of T_{dust} from $z=0$ to $z \sim 6-7$. Using an analytic model with parameters consistent with recent James Webb Space Telescope results, we discuss that the observed redshift evolution of the dust temperature can be reproduced by an ~ 0.6 dex decrease in the gas depletion timescale and ~ 0.4 dex decrease in the metallicity. The variety of T_{dust} observed at high redshifts can also be naturally explained by scatters around the star formation main sequence and average mass-metallicity relation including an extremely high dust temperature of $T_{\text{dust}} > 80$ K observed in a galaxy at $z = 8.3$.


Unified Astronomy Thesaurus concepts: [Galaxy evolution \(594\)](#); [Galaxy formation \(595\)](#); [High-redshift galaxies \(734\)](#)

1. Introduction

The cosmic star formation rate density (SFRD) is one of the most important quantities to understand the evolution of galaxies as well as the history of the Universe. Over recent decades, the SFRD has been derived through the ultraviolet (UV) emission of galaxies from the present day ($z=0$) to $z \sim 12$ by utilizing ground-based and space telescopes such as the Canada-France-

Hawaii Telescope, Keck Telescope, Subaru Telescope, Hubble Space Telescope (HST), and James Webb Space Telescope (JWST; e.g., Lilly et al. 1996; Madau et al. 1996; Steidel et al. 1999; Bouwens et al. 2007, 2015; Bouwens et al. 2023a; Bouwens et al. 2023b; Oesch et al. 2010, 2013; Coe et al. 2013; Ellis et al. 2013; Finkelstein et al. 2015; Moutard et al. 2020; Harikane et al. 2023a, 2024). These observations revealed that the SFRD traced by rest-frame UV emission peaks at $z \sim 2-3$ and subsequently declines toward the early Universe (Madau & Dickinson 2014, and references therein).

Given that the UV radiation from young massive stars within galaxies is easily absorbed by interstellar dust, it is necessary to

 Original content from this work may be used under the terms of the [Creative Commons Attribution 4.0 licence](#). Any further distribution of this work must maintain attribution to the author(s) and the title of the work, journal citation and DOI.

measure both direct and reprocessed stellar emission corresponding to both the rest-frame UV and the rest-frame far-infrared (FIR), respectively. The dust-obscured SFRD is explored with FIR to submillimeter observatories such as Spitzer, Herschel, and the James Clark Maxwell Telescope, revealing a monotonic increase by an order of magnitude from $z=0$ to $z\sim 2$ (e.g., Chary & Elbaz 2001; Magnelli et al. 2009, 2011, 2013). However, at $z > 4$, the dust-obscured SFRD is poorly constrained, with the discrepancy among studies reaching nearly 2 orders of magnitude (Robertson et al. 2010; Gruppioni et al. 2020; Casey et al. 2021; Fudamoto et al. 2021; Khusanova et al. 2021; Zavala et al. 2021; Algera et al. 2023; Barrufet et al. 2023a; Fujimoto et al. 2023). The relation between IRX ($\text{IRX} \equiv L_{\text{IR}}/L_{\text{UV}}$) and the UV spectral slope (β_{UV}) can be used to correct for the dust-absorbed UV emission in the absence of the FIR/submillimeter observations. Since this relationship is useful for inferring the total (UV+IR) star formation activity of galaxies from the rest-frame UV observations alone, it has been extensively explored using several types of local galaxies such as local starbursts (Meurer et al. 1999; Calzetti et al. 2000; Takeuchi et al. 2012) and the Small Magellanic Cloud (SMC; Gordon et al. 2003), and galaxies at $z \sim 1-3$ (Reddy et al. 2015, 2018; Álvarez-Márquez et al. 2016, 2019). With the advent of the Atacama Large Millimeter-submillimeter Array (ALMA), some studies have investigated the IRX- β_{UV} relation at $z > 4$. For example, Fudamoto et al. (2020a) examined the IRX- β_{UV} relation at $z \sim 5$, and found a redshift evolution at $z > 4$ (see also Capak et al. 2015; Barisic et al. 2017; Faisst et al. 2017). Recent ALMA observations toward $z \sim 7$ UV-selected galaxies suggest a significant contribution of the dust-obscured star formation at high redshift (Fudamoto et al. 2021; Algera et al. 2023; Barrufet et al. 2023a).

While these ALMA studies shed light on the dust-obscured star formation at $z > 4$, the IR luminosity depends on their assumption of the shape of FIR spectral energy distribution (SED). The variations in FIR SEDs are challenging to account for at $z > 4$ due to sensitivity limitations in observing the peak of dust thermal emission at mid-IR-to-FIR wavelengths in the observed frame. As the FIR SED might depend on the UV slope β_{UV} (e.g., Álvarez-Márquez et al. 2019), considering its variation is essential for constructing an accurate IRX- β_{UV} relationship. Specifically, the luminosity-weighted dust temperature (T_{dust}) is one of the key parameters that determine the shape of the FIR SEDs. For instance, the dust temperature severely affects estimates of L_{IR} and therefore the dust-obscured star formation rate (SFR). Moreover, in the case of the UV-to-FIR SED modeling based on the energy balance principle with a single ALMA observation, the assumed T_{dust} can influence inferred stellar ages or metallicities due to the degeneracy with dust attenuation. While there is observational (e.g., Magnelli et al. 2014; Béthermin et al. 2015; Schreiber et al. 2018; Faisst et al. 2020a; Sommovigo et al. 2021, 2022; Viero et al. 2022) and theoretical (e.g., Ferrara et al. 2017; Liang et al. 2019; Ma et al. 2019; Sommovigo et al. 2020) evidence suggesting higher T_{dust} in higher- z galaxies, the redshift dependence at $z \gtrsim 5$ is still unclear because of the limited sample size (Faisst et al. 2020a; Akins et al. 2022; Witstok et al. 2022; Algera et al. 2023). Theoretical and analytical studies suggest that T_{dust} could be related to galaxies' metal content or star formation surface densities (Liang et al. 2019; Ma et al. 2019; Sommovigo et al. 2022), although this

has not been confirmed observationally. Hence, obtaining representative T_{dust} values and examining the potential origin of its variation is essential as a prior assumption to calculate SFR and L_{IR} .

In this paper, we examine the FIR property of galaxies at $z \sim 6$ with our new ALMA Band 6/8 observations toward 11 Lyman break galaxies (LBGs) at $z_{\text{spec}} \sim 6$. The ALMA Band 8, covering rest-frame $\sim 90 \mu\text{m}$ dust continuum near the peak of the dust thermal emission at $z \sim 6$, enables us to constrain T_{dust} . In addition to individual measurements, stacking analysis can derive an IRX- β_{UV} relationship with the consideration of the variety of the FIR SEDs at $z \sim 6$. We aim to inform the IRX- β_{UV} relation at $z \sim 6$ by comparing our multiband analysis with single-band measurements in the literature. We also examine the representative T_{dust} with a statistically significant number of $z \sim 5-8$ galaxies by compiling our new observations and archival data of additional 14 galaxies at $z = 5-8$. We reanalyze the archival data in a homogeneous way to our target galaxies at $z \sim 6$ for a fair comparison. An observational attempt to constrain T_{dust} and their evolution yields fundamental information to understand the dust-obscured star formations in the early Universe.

The paper is organized as follows: Section 2 provides an overview of the data sets used in this work. Section 3 describes the method of measurements for UV and IR properties, and shows the parameter coverage of this work compared with previous studies. In Section 4, we report the IRX- β_{UV} and $M_{\text{UV}}-f_{\text{obs}}$ relations, the contribution of the dust-obscured star formation at $z \sim 6$, and the results of T_{dust} measurements. Discussions of the model of T_{dust} evolution are described in Section 5. The conclusions are presented in Section 6. Throughout this paper, we assume a flat universe with the cosmological parameters of $\Omega_{\text{M}} = 0.3$, $\Omega_{\Lambda} = 0.7$, $\sigma_8 = 0.8$, and $H_0 = 70 \text{ km s}^{-1} \text{ Mpc}^{-1}$.

2. Observation and Data

2.1. SERENADE Overview

Systematic Exploration in the Reionization Epoch using Nebular And Dust Emission (SERENADE) is an ALMA program (ID: #2022.1.00522.S, PI: Y. Harikane) designed to observe the two brightest FIR fine structure lines ([C II] $158 \mu\text{m}$ and [O III] $88 \mu\text{m}$) from LBGs at $z \sim 6$. The parent sample of the target galaxies is selected from the literature, mostly from the galaxy sample identified in Hyper Suprime-Cam Subaru Strategic Program (HSC-SSP; Matsuoka et al. 2016, 2018a, 2018b; Aihara et al. 2018; Ono et al. 2018; Harikane et al. 2022), based on the following four criteria: (1) spectroscopic confirmation of their redshifts, (2) redshifted [O III] $88 \mu\text{m}$ and Ly α falling into ALMA Band 8 and ground-based optical telescopes, respectively ($z = 5.8-6.3$), (3) the absence of clear active galactic nuclei (AGN)/QSO signatures in their rest-frame UV spectra, and (4) sufficient expected brightness for the detection of emission lines within a relatively short observing time ($\lesssim 10 \text{ hr}$). We select 19 galaxies as our targets to encompass a broad dynamic range in an SFR or a rest-frame UV absolute magnitude (M_{UV} , see Figure 1), including two lensed galaxies (see Table 1). The targeting SERENADE galaxies have almost similar or slightly smaller M_{UV} than the ALPINE (Le Fèvre et al. 2020) or REBELS galaxies (Bouwens et al. 2022). Observations were conducted between 2022 October and December using the C43-1/2/3 configuration.

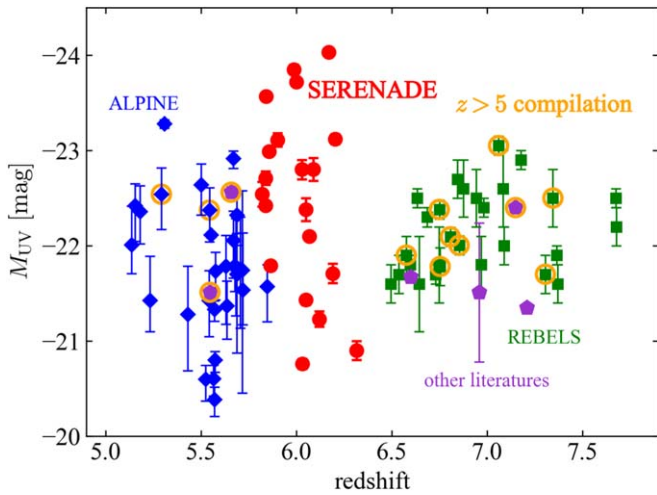


Figure 1. Rest-frame UV absolute magnitude of the SERENADEX galaxies (red), the ALPINE galaxies (blue; Fudamoto et al. 2020a; Le Fèvre et al. 2020), the REBELS galaxies (green; Bouwens et al. 2022; Inami et al. 2022), and those of the other literature (purple; Hashimoto et al. 2019; Bakx et al. 2021; Akins et al. 2022; Witstok et al. 2022; Algera et al. 2023). The literature galaxies with multiband ALMA observations reanalyzed in this paper are surrounded by orange circles (see Section 2.2).

Since one targeting galaxy (J023536-031737) was not observed in either Band 6 or Band 8, we address the remaining 18 LBGs in this paper. Among 18 LBGs, 11 are observed in both $158\ \mu\text{m}$ and $88\ \mu\text{m}$.

We have also incorporated three galaxies reported in Harikane et al. (2020b) for the $z \sim 6$ galaxy sample with $158\ \mu\text{m}$ and $88\ \mu\text{m}$ coverage. In total, the SERENADEX galaxies are composed of 21 galaxies (18 galaxies in Cycles 9 and 3 galaxies in the pilot study in Harikane et al. 2020b) at $z \sim 6$, including 14 galaxies (11 from Cycles 9 and 3 from Harikane et al. 2020b) with the $158\ \mu\text{m}$ and $88\ \mu\text{m}$ coverage. Among the 21 target galaxies, observations were conducted for 20 [C II] and 15 [O III] emission lines. Of these, 16 [C II] and 10 [O III] emission lines were detected with a signal-to-noise ratio (S/N) greater than 3. A comprehensive discussion of the emission line data is beyond the scope of this paper and will be provided in an upcoming paper (Paper I; Y. Harikane et al. 2024, in preparation). Regarding the dust continuum emission, the main focus of this paper, 14 galaxies are covered at both rest-frame $158\ \mu\text{m}$ and $88\ \mu\text{m}$. Of these, six galaxies are detected in both wavelengths, two galaxies are only detected at $158\ \mu\text{m}$, and six galaxies are detected at neither $158\ \mu\text{m}$ nor $88\ \mu\text{m}$. There are also six galaxies observed solely in $158\ \mu\text{m}$ and one in $88\ \mu\text{m}$. We provide more details on the continuum detection and flux measurements in Section 3.3.

2.2. Additional $5 < z < 8$ Samples

We incorporate an additional 14 galaxies at $5 < z < 8$ with multiband ALMA coverage in this study: four galaxies at $z \sim 5$ (Faisst et al. 2020a), and 10 galaxies at $z \sim 7$ (Watson et al. 2015; Knudsen et al. 2017; Hashimoto et al. 2019; Inoue et al. 2020; Bakx et al. 2021; Sugahara et al. 2021; Akins et al. 2022; Witstok et al. 2022; Algera et al. 2023). We collect galaxies at $5 < z < 8$ with both Band 6 and Band 8 observations publicly available in the ALMA science archive. For a fair comparison, we reanalyze these data sets in the same manner as the SERENADEX galaxies. The differences between our measurement and previous studies mainly come from the flux

measurement methodology, but we note that our results are broadly consistent with the previously mentioned studies.

2.3. Summary of the Samples

In total, we have 28 galaxies with multiband ALMA coverage composed of 14 SERENADEX galaxies and the additional 14 galaxies at $5 < z < 8$ in the literature. Among 28 galaxies, 21 are individually detected in at least one band, allowing us to estimate T_{dust} or constrain the upper limit of T_{dust} . This is the largest sample of $z \gtrsim 5$ galaxies with multiband dust continuum observation.

3. Analysis

3.1. Measurement of β_{UV} and M_{UV}

To compare the dust continuum properties with the rest-frame UV continuum properties, we estimate parameters that characterize the UV continuum, such as UV continuum slope (β_{UV} ; $f_{\lambda} \propto \lambda^{\beta_{\text{UV}}}$) and absolute magnitude (M_{UV}). The slope of the UV spectrum is mainly determined by the stellar age, stellar metallicity, and the amount of dust attenuation. Our calculations utilize broadband photometry spanning a rest-frame wavelength range as large as $800\text{--}3000\ \text{\AA}$ depending on the data availability at the position of each galaxy. All of the utilized photometries, along with their references, are listed in Table 1. We crossmatch catalog coordinates with the central coordinate of our target galaxies derived from the detection in previous papers. For galaxies residing in the Cosmic Evolution Survey (COSMOS Scoville et al. 2007), Subaru/XMM-Newton Deep Field (SXDF; Pierre et al. 2004), and XMM Large Scale Structure survey (Pierre et al. 2004), we obtain i , z , J , H , and K -band photometries from the latest COSMOS2020 catalog (Weaver et al. 2022), SPLASH-SXDF multiwavelength catalog (Mehta et al. 2018), and VISTA Deep Extragalactic Observations catalog (Jarvis et al. 2013), respectively. We take i , z , and y -band photometry from the HSC-PDR3 catalog (Aihara et al. 2022) for the galaxies originally identified in the wide layer of the HSC-SSP survey (Aihara et al. 2018). If the galaxies are covered in the United Kingdom Infrared Telescope Deep Sky Survey (Lawrence et al. 2007) or VISTA Kilo-degree Infrared Galaxy survey (Jarvis et al. 2013), we combine the photometries at near-infrared (NIR) wavelengths with the i , z , and y -band photometry following Matsuoka et al. (2019). For galaxies not covered by the aforementioned catalogs, we refer to the photometries measured in the literature (mostly from HST observations, e.g., Smit et al. 2018), or directly adopt β_{UV} and/or M_{UV} values (e.g., Huang et al. 2016) when the photometries are not publicly available.

We fit the broadband photometry from the catalogs to estimate β_{UV} and M_{UV} , assuming a simple power-law spectral shape described by $f_{\lambda} \propto \lambda^{\beta_{\text{UV}}}$ with a truncation at $\lambda_{\text{rest}} = 1216\ \text{\AA}$ corresponding to the intergalactic medium absorption by H I gas. We take into account the contribution of the Ly α emission line if the line is clearly detected in the spectroscopic observations. The brightness of the Ly α line is obtained from the literature or calculated from spectra following the methodologies in Harikane et al. (2020b). We fit model UV SEDs created with the logarithmic ranges of $[-0.5, 0.5]$ for the normalization flux in the y band and $[-5, 3]$ for the UV slope β_{UV} . From each set of parameters, we derive M_{UV} by interpolating the model spectrum to the rest frame of $1500\ \text{\AA}$. The best-fit value and associated 1σ uncertainty of β_{UV}

Table 1
Summary of the Parameters Related to Rest-frame UV Spectra

ID	z_{spec}^a	i^b (mag)	z^b (mag)	y, Y, Y_{110}^b (mag)	J, J_{125}^b (mag)	H, H_{160}^b (mag)	K_s (mag)	$\text{EW}_{\text{Ly}\alpha}^0$ (Å)	M_{1500} (mag)	β_{UV}	References
SERENADE (Cycle 9)											
J020038-021052	6.1120	≥ 26.7	23.69 ± 0.06	≥ 25.2	542.23	≥ -21.5	≤ 2.03	(1, 2)
J021033-052304	5.9007	25.85 ± 0.17	23.78 ± 0.06	23.54 ± 0.11	-23.11 ± 0.07	$0.25_{-1.05}^{+1.29}$	(1, 3, 4)
J021041-055917	5.8216	26.61 ± 0.27	24.25 ± 0.27	24.10 ± 0.16	-22.54 ± 0.13	$-0.64_{-2.91}^{+3.15}$	(1, 3)
J021244-015824	6.00	25.53 ± 0.17	23.23 ± 0.03	22.96 ± 0.06	-23.72 ± 0.04	$0.33_{-0.48}^{+0.65}$	(1, 4)
J021735-051032	6.12	...	25.16 ± 0.11	25.40 ± 0.26	25.68 ± 0.19	26.03 ± 0.46	25.81 ± 0.28	46.8 ± 8.4	-21.23 ± 0.08	$-2.49_{-0.24}^{+0.24}$	(6, 7)
J021807-045841	6.0446	28.04 ± 0.61	25.10 ± 0.07	25.07 ± 0.14	25.54 ± 0.13	25.62 ± 0.24	26.48 ± 0.38	27.6 ± 4.1	-21.43 ± 0.05	$-2.9_{-0.24}^{+0.16}$	(6, 7)
J021838-050943	6.1860	...	25.08 ± 0.17	24.74 ± 0.25	25.02 ± 0.15	24.93 ± 0.22	25.11 ± 0.21	39.4 ± 6.0	-21.71 ± 0.10	$-2.01_{-0.16}^{+0.24}$	(6, 7)
J022023-050431	5.8403	24.22 ± 0.04	24.29 ± 0.08	24.33 ± 0.12	24.29 ± 0.19	...	-22.42 ± 0.03	$-2.17_{-0.08}^{+0.16}$	(8, 9)
J022627-045238	6.0675	...	24.77 ± 0.04	24.42 ± 0.04	24.78 ± 0.10	24.28 ± 0.09	25.06 ± 0.27	13.0 ± 4.0	-22.10 ± 0.01	$-1.61_{-0.08}^{+0.08}$	(9, 10)
J024801-033258 ^c	6.0271	26.4 ± 0.1	25.7 ± 0.1	25.30 ± 0.09	25.5 ± 0.1	25.2 ± 0.1	...	21.1 ± 2.8	-20.76 ± 0.05	$-1.44_{-0.16}^{+0.16}$	(11, 12)
J045408-030014 ^c	6.3163	8.2 ± 1.4	-20.9 ± 0.1	-1.6 ± 0.2	(13)
J085723+014254	5.8394	26.24 ± 0.26	24.14 ± 0.05	23.93 ± 0.09	5.1 ± 0.1	-22.71 ± 0.07	$0.01_{-0.89}^{+0.97}$	(1, 3)
J091436+044231	5.8433	25.46 ± 0.12	23.29 ± 0.06	23.07 ± 0.08	-23.57 ± 0.04	$0.09_{-0.89}^{+0.97}$	(1, 14)
J100008+021136	5.8650	26.29 ± 0.05	24.91 ± 0.03	24.78 ± 0.04	24.86 ± 0.05	24.84 ± 0.07	25.00 ± 0.10	31.5 ± 27.0	-21.79 ± 0.01	$-2.01_{-0.01}^{+0.01}$	(15, 16)
J100634+030005	5.8588	25.79 ± 0.10	23.70 ± 0.02	23.65 ± 0.05	-22.99 ± 0.03	$-1.61_{-0.40}^{+0.57}$	(1, 14)
J114412-000613	6.05	≥ 26.1	24.63 ± 0.10	24.32 ± 0.15	-22.38 ± 0.12	$0.25_{-1.70}^{+1.86}$	(1, 8)
J135348-001026	6.1702	27.25 ± 0.44	23.33 ± 0.03	22.65 ± 0.03	22.15 ± 0.26	...	20.78 ± 0.16	...	-24.03 ± 0.03	$0.49_{-0.16}^{+0.08}$	(1, 17)
J142824+015934	5.9881	26.05 ± 0.43	22.90 ± 0.05	22.83 ± 0.07	-23.85 ± 0.05	$-1.61_{-0.73}^{+0.89}$	(1, 14)
SERENADE pilot (Harikane et al. 2020b)											
J1211+0118	6.0293	27.82 ± 0.76	23.95 ± 0.05	23.92 ± 0.09	6.9 ± 0.8	-22.80 ± 0.10	$-1.61_{-1.13}^{+0.81}$	(1, 14)
J0217+0208	6.2037	≥ 26.7	23.90 ± 0.04	23.61 ± 0.08	15.0 ± 1.0	-23.12 ± 0.05	$-1.20_{-0.81}^{+1.05}$	(1, 14)
J0235+0532	6.0901	27.40 ± 0.65	23.81 ± 0.06	23.89 ± 0.14	41.0 ± 2.0	-22.80 ± 0.12	$-0.56_{-1.21}^{+1.45}$	(1, 14)
$z \sim 7$ LBGs (Hashimoto et al. 2019; Bakx et al. 2021; Akins et al. 2022; Witstok et al. 2022; Algera et al. 2023)											
COS- 2987030247	6.8076	27.61 ± 0.22	28.46 ± 0.81	25.08 ± 0.07	24.99 ± 0.05	24.81 ± 0.06	24.60 ± 0.08	...	-21.92 ± 0.05	$-1.36_{-0.08}^{+0.16}$	(16, 18)
COS-3018555981	6.854	≥ 27.6	...	25.65 ± 0.11	24.98 ± 0.04	25.09 ± 0.07	25.24 ± 0.12	...	-21.91 ± 0.02	$-2.41_{-0.16}^{+0.16}$	(16, 18)
UVISTA-Z-001	7.0611	27.44 ± 0.21	...	25.10 ± 0.08	23.98 ± 0.02	24.02 ± 0.03	23.83 ± 0.04	...	-22.96 ± 0.01	$-1.85_{-0.01}^{+0.01}$	(16, 19)
UVISTA-Z-007	6.7498	28.20 ± 0.40	28.55 ± 0.95	24.75 ± 0.06	24.74 ± 0.04	24.76 ± 0.06	24.61 ± 0.08	...	-22.13 ± 0.02	$-1.85_{-0.08}^{+0.08}$	(16, 19)
UVISTA-Z-019	6.7544	29.03 ± 0.79	...	25.72 ± 0.13	25.07 ± 0.05	25.21 ± 0.08	25.09 ± 0.12	...	-21.80 ± 0.06	$-2.17_{-0.16}^{+0.16}$	(16, 19)
A1689-zD1	7.133	25.00 ± 0.13	24.64 ± 0.05	24.51 ± 0.11	-22.34 ± 0.02	$0.01_{-0.73}^{+0.73}$	(20, 21, 22)
B14-65666	7.1521	24.7 ± 0.2	24.6 ± 0.3	-22.29 ± 0.18	$-1.69_{-1.21}^{+1.21}$	(23, 24)
REBELS-12	7.3459	...	26.03 ± 0.12	24.92 ± 0.06	24.21 ± 0.06	24.74 ± 0.14	24.14 ± 0.11	...	-22.76 ± 0.02	$-2.09_{-0.16}^{+0.24}$	(25, 26)
REBELS-25	7.3065	...	29.08 ± 1.63	27.23 ± 0.59	25.44 ± 0.08	25.22 ± 0.10	24.45 ± 0.18	...	-21.53 ± 0.05	$-0.64_{-0.24}^{+0.24}$	(25, 26)
REBELS-38	6.5770	≥ 27.6	26.88 ± 0.23	25.00 ± 0.09	25.00 ± 0.17	24.84 ± 0.20	25.00 ± 0.16	...	-21.87 ± 0.03	$-2.01_{-0.32}^{+0.32}$	(25, 26)
$z \sim 5.5$ LBGs (Faisst et al. 2020b)											
HZ4	5.544	24.77 ± 0.02	24.03 ± 0.02	24.05 ± 0.03	24.24 ± 0.11	23.81 ± 0.10	24.32 ± 0.10	...	-22.53 ± 0.01	$-2.09_{-0.08}^{+0.01}$	(16, 27, 28)
HZ6	5.293	24.40 ± 0.02	23.62 ± 0.02	23.58 ± 0.03	23.47 ± 0.02	23.35 ± 0.02	23.26 ± 0.03	...	-22.90 ± 0.01	$-1.61_{-0.01}^{+0.01}$	(16, 27, 28)

4

Table 1
(Continued)

ID	$z_{\text{spec}}^{\text{a}}$	i^{b} (mag)	z^{b} (mag)	y, Y, Y_{110}^{b} (mag)	J, J_{125}^{b} (mag)	H, H_{160}^{b} (mag)	K_s (mag)	$\text{EW}_{\text{Ly}\alpha}^0$ (Å)	M_{1500} (mag)	β_{UV}	References
HZ9	5.541	25.67 ± 0.03	24.83 ± 0.03	24.93 ± 0.05	24.21 ± 0.07	24.50 ± 0.12	24.51 ± 0.09	...	-21.80 ± 0.01	$-1.44^{+0.08}_{-0.08}$	(16, 27, 28)
HZ10	5.657	25.68 ± 0.04	24.50 ± 0.03	24.38 ± 0.04	-22.20 ± 0.01	$-0.88^{+0.57}_{-0.40}$	(16, 27, 28)

Notes.

^a The difference in the number of decimal places reflects the precision. For instance, the redshifts of the SERENADE galaxies determined by [C II]/[O III] emission lines and Ly α emission/UV absorption lines have four and two decimals, respectively.

^b The izy , $Y_{110}J_{125}H_{160}$, and YHK_s represent the Subaru/HSC, HST, and VISTA photometric bands, respectively.

^c Lensed galaxies. Lens magnification factors are 2.5 and 4.4 for J024801-033258 and J045408-030014, respectively (Bradley et al. 2014; Huang et al. 2016). The absolute magnitudes, M_{UV} , are corrected for the magnification factors, while the observed magnitudes are not.

References. (1) Aihara et al. (2022), (2) Y. Ono et al. (2024, in preparation), (3) Matsuoka et al. (2016), (4) Harikane et al. (2020b), (5) Matsuoka et al. (2018b), (6) Curtis-Lake et al. (2012), (7) Mehta et al. (2018), (8) M. Sawicki et al. (2024, in preparation), (9) Jarvis et al. (2013), (10) Willott et al. (2015), (11) Mainali et al. (2018), (12) Bradley et al. (2014), (13) Huang et al. (2016), (14) Matsuoka et al. (2018a), (15) Mallery et al. (2012), (16) Weaver et al. (2022), (17) Matsuoka et al. (2019), (18) Smit et al. (2018), (19) Schouws et al. (2022), (20) Watson et al. (2015), (21) Wong et al. (2022), (22) Akins et al. (2022), (23) Bowler et al. (2014), (24) Hashimoto et al. (2019), (25) Bouwens et al. (2022), (26) Algera et al. (2023), (27) Capak et al. (2015), (28) Faisst et al. (2020b).

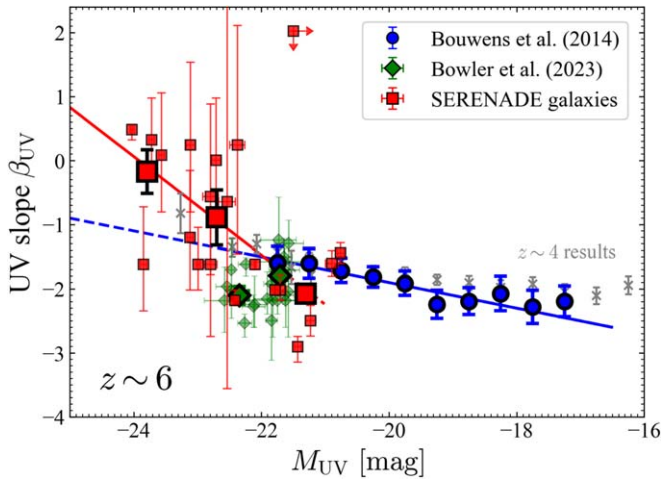


Figure 2. Relationship between the rest-frame UV absolute magnitude and UV slope β_{UV} . The SERENADE galaxies (red-filled squares) are typically brighter than the binned results of HST-identified galaxies (blue points; B14). Our bright galaxies with $M_{UV} < -22.0$ mag generally exhibit redder slopes than the extrapolation of the relation constrained with faint galaxies in B14. Such a trend at the bright end has also been reported in previous studies at $z \sim 4$ (gray crosses; Lee et al. 2011; B14; see also Yamanaka & Yamada 2019).

and M_{UV} are derived as the value showing the minimum χ^2 and the deviation at which $\Delta\chi^2 = 1$ from the minimum χ^2 value, respectively. We find a typical reduced χ^2 value is $\chi^2_v = 3.0$, except for the sources covered in two photometric bands.

3.2. M_{UV} versus β_{UV} Relationship

In Figure 2, we plot individual galaxy measurements of M_{UV} - β_{UV} and representative average data points by binning our galaxies into three M_{UV} bins of $[-24.5:-23.5]$, $[-23.5:-22.0]$, and $[-22.0:-20.5]$. The error bar represents a 1σ standard deviation of the sample. This result is consistent with the previous results, supporting the idea that more UV-luminous star-forming galaxies have redder UV slope β_{UV} (e.g., Reddy et al. 2010; Bouwens et al. 2014; Yamanaka & Yamada 2019). The UV slope could be redder than the extrapolated following relationship normalized in $M_{UV} = -19.5$ mag at $z \sim 6$:

$$\beta_{UV} = -(2.00 \pm 0.09)(M_{UV} + 19.5) - (0.20 \pm 0.07) \quad (1)$$

from Bouwens et al. (2014, hereafter B14) at $M_{UV} < -22.0$ mag. Such a bending trend at the bright end has been reported in previous studies (e.g., Lee et al. 2011). Our best-fit linear M_{UV} - β_{UV} relationship normalized in $M_{UV} = -22$ mag is represented as the following:

$$\beta_{UV} = -(0.76 \pm 0.14)(M_{UV} + 22) - (1.51 \pm 0.15). \quad (2)$$

In contrast, Bowler et al. (2024) show potential flattening or turnover at $M_{UV} < -21.5$ mag, which may originate from a low dust obscuration due to clumpy geometry of the REBELS galaxies.

The Lyman break selection technique could introduce biases favoring blue galaxies (i.e., small β_{UV}). The typical i -dropout selection criteria are composed of not only a red $i-z$ color to identify the Lyman break but also a blue $z-y$ color coming from blue UV continuum (e.g., Bouwens et al. 2012, B14; Harikane et al. 2022, see also Steidel et al. 1999). For example, the selection criteria used in Bouwens et al. (2012) select galaxies with $\beta_{UV} \lesssim 0.5$ at $z \sim 5.8-6.3$. Given that our target

galaxies are collected from a variety of surveys, potential biases could permeate our results. While it is difficult to evaluate the biases on the M_{UV} - β_{UV} relationship, we test the potential bias by limiting galaxies selected from Subaru High- z Exploration of Low-luminosity Quasars (SHELLQs) survey and follow-up spectroscopic observations. As the galaxies from the SHELLQs survey are selected without any color criteria on the UV slope β_{UV} (see Figure 11 in Matsuoka et al. 2018b), the galaxy sample offers a more homogeneous selection compared to the galaxies culled from surveys external to the SHELLQs.²¹ As a result, there is no major change if we calculate the average values only with the galaxies from the SHELLQs survey. Consequently, we conclude that the overall trend is authentic although enlarging the sample size is imperative to draw robust conclusions. Note that an average in the range $M_{UV} \geq -22$ mag may be biased to bluer β_{UV} since all five galaxies in this range originate from inhomogeneous surveys.

3.3. Dust Continuum Fluxes

In this section, we describe the detection and measurement of the dust continuum fluxes. First, we make data cubes with the taper scale of $1''0$ and apply a single Gaussian fitting to the spectra extracted at the phase center to identify [C II] $158 \mu\text{m}$ or [O III] $88 \mu\text{m}$ emission lines. If any emission line feature is identified (i.e., Gaussian fitting converges), we mask a frequency range that is three times wider than the line velocity dispersion using CASA/MSTRANSFORM. For cases with non-detection, we exclude the frequencies at ± 0.8 GHz (equivalent to $\pm 500 \text{ km s}^{-1}$) from the expected central frequency from their prior redshift to ensure eliminating potential emission line contamination to the dust continuum. Subsequently, we generate continuum images with CASA/TCLEAN. To recover all possible extended structures, we reconstruct images with uv taper of $0''.25$, $0''.5$, $1''.0$, $2''.0$, and $3''.0$ in addition to the naturally weighted image without tapering. We obtain peak flux density within a $0''.5$ radius from each galaxy's central position, under the assumption that dust continuum emission is included within a single beam. Noise levels are estimated in the images without primary beam corrections as the rms of pixel values within the field of view where the primary beam correction value exceeds 0.5. As the fiducial S/N of each galaxy, we adopt the highest S/N among the images. Galaxies with a fiducial S/N > 3.5 in any band are considered as continuum detection.

Figure 3 shows the thumbnails of the SERENADE galaxies. The contours of the naturally weighted dust continuum in the rest-frame $158 \mu\text{m}$ (red) and $88 \mu\text{m}$ (blue) are overlaid on the HSC z -band or HST $Y_{105}J_{125}H_{160}$ combined images. Of the 14 galaxies observed in both Band 6 and Band 8, six galaxies are detected in both the rest-frame $158 \mu\text{m}$ and $88 \mu\text{m}$, two galaxies are only detected in the rest-frame $158 \mu\text{m}$ dust continuum, and six galaxies are not detected in $158 \mu\text{m}$ nor $88 \mu\text{m}$. There are also six galaxies observed solely in Band 6 and one in Band 8.

We measure the total flux density at multiple frequencies with consideration for the different spatial resolutions between the rest-frame $158 \mu\text{m}$ and $88 \mu\text{m}$ continuum. To ensure that the total fluxes are measured and to achieve uniform

²¹ As the selection of $z \sim 6$ quasars in the SHELLQs survey is composed of the red color originating from the Lyman break ($i-z > 1.5$) and the compactness, there may be other biases apart from the UV slope (see Matsuoka et al. 2016, for more details).

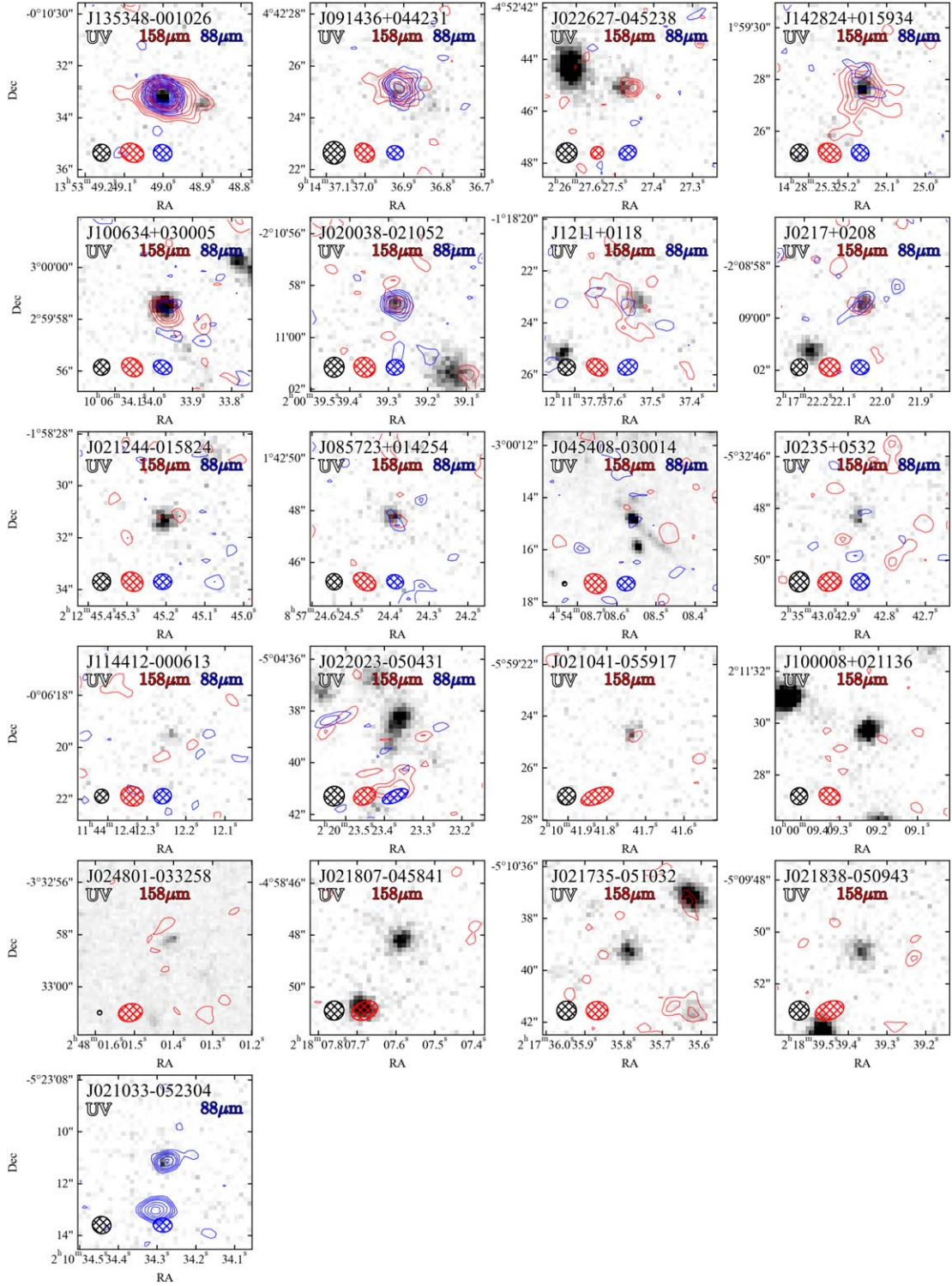


Figure 3. Thumbnails of the SERENA galaxies. The red and blue contours indicate rest-frame $158\ \mu\text{m}$ and $88\ \mu\text{m}$ dust continua, respectively. The contours are shown every 1σ from 3σ to 5σ and every 2σ from 5σ . The background images are HST $Y_{105}J_{125}H_{160}$ combined images for J024801-033258 and J045408-030014 and Subaru/HSC z -band images for others. The source ID and beam sizes in each wavelength are also shown.

measurements across frequencies, we employ the following three methods to calculate fiducial flux values: (1) For the galaxies detected in both rest-frame $158\ \mu\text{m}$ and $88\ \mu\text{m}$, we execute CASA/IMFIT, (2) for those detected only in $158\ \mu\text{m}$, we get the peak flux density and rms in images with uv taper of $1''0$ following the S/N calculations described above, and (3) for the galaxies not detected in any bands, we calculate upper

limits from the naturally weighted images. The reason behind method (2) is to ensure uniformity in the calculation of the rms levels between the detected and undetected frequencies. To avoid the flux misestimation in IMFIT due to the mismatch of dirty and clean beams, we apply modest tapers for some sources before running IMFIT. From the comparison between the fiducial flux value calculated above and the total flux

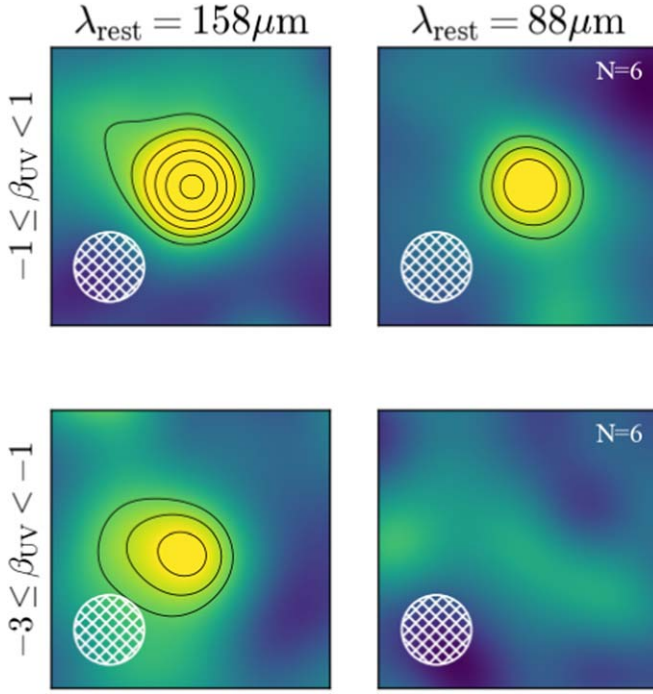


Figure 4. $6'' \times 6''$ cutout of the stacked images in both rest-frame $158 \mu\text{m}$ and $88 \mu\text{m}$. We show the number of galaxies included in each bin and the representative beam sizes of each stacked image. The contour levels are every 1σ starting from 3σ .

derived from the visibility analysis presented in the [Appendix](#), we find that calculated fiducial fluxes, in any case, are consistent with those from the visibility analysis. We also find that CASA/IMFIT achieves better flux recovery than that from the images with the multiple taper scales. These comparisons are shown in [Figure 11](#) in the [Appendix](#).

3.4. Stacking Analysis

In this section, we stack the dust continuum of the SERENADE galaxies at $z \sim 6$ to obtain an average representation that is not biased by individual detection. We perform the stacking of both rest-frame $88 \mu\text{m}$ and $158 \mu\text{m}$ dust continua from galaxies in two distinct β_{UV} bins of $\beta_{\text{UV}} = [-3, -1]$ and $[-1, 1]$, where each bin includes approximately an equal number of galaxies. Only galaxies observed in both Band 6 and Band 8 are used in the stacking analysis for the sake of homogeneity. Additionally, we exclude two galaxies (J020038-021052 and J024801-033258) because J020038-021052 does not have an M_{UV} estimation and J024801-033258 is lensed. The resulting stacked images are shown in [Figure 4](#). Given the variable nature of the ALMA beam sizes, we construct continuum images with a round $2''.0$ beam by applying CASA/IMSMOOTH for the images with a prior $1''$ taper. For the reference position of the stacking, we use central positions derived in the rest-frame UV continuum (i.e., phase center of the ALMA observations). We note that spatial offsets identified in individual galaxies between UV and IR do not significantly impact the flux measurement since the spatial offsets are less than $0''.35$. Then we also compute the weighted average with the following weight based on the UV luminosity of i th galaxy

in the sample:

$$w_i = \frac{L_{\text{UV}}^{\text{mean}}}{L_{\text{UV},i}}. \quad (3)$$

This reciprocal weighting with respect to L_{UV} allows us to avoid bias toward bright galaxies. Finally, we measure fluxes with the same procedure described in [Section 3.3](#). We find that there is no major difference when we use the weighted median instead of the weighted average.

3.5. T_{dust} and L_{IR} Estimation

We fit a modified blackbody (MBB) to constrain the properties of the dust emission. The MBB profile is mainly determined by three parameters: dust temperature (T_{dust}), dust mass (M_{dust}), and emissivity of the dust grain (β_{dust}). The general formulation of the observed MBB flux density at ν_{obs} is as follows:

$$F_{\nu_{\text{obs}}} = \left(\frac{1+z}{d_L^2} \right) \left(\frac{1 - e^{-\tau_\nu}}{\tau_\nu} \right) M_d \kappa_\nu B_\nu(T_{\text{dust}}). \quad (4)$$

Here d_L and τ_ν are the luminosity distance at redshift z and the optical depth of the dust grain, respectively. $B_\nu(T_{\text{dust}})$ represents the blackbody radiation at the temperature of T_{dust} . The absorption coefficient κ_ν is assumed by $\kappa_\nu = \kappa_*(\nu/\nu_*)^{\beta_{\text{dust}}}$ with the normalization of Milky Way value, $[\kappa_*, \nu_*] = [10.41 \text{ cm}^{-2} \text{ g}^{-1}, 1900 \text{ GHz}]$ (e.g., [Bakx et al. 2021](#); [Ferrara et al. 2022](#); [Algera et al. 2023](#)). The dust optical depth is defined by the net absorption over the line of sight and represented as $\tau_\nu = \kappa_\nu \Sigma_{\text{dust}}$, where Σ_{dust} represents the surface dust mass density. τ_ν is also commonly written as $(\nu/\nu_0)^\beta = (\lambda_0/\lambda)^\beta$, where ν_0 is a frequency at which the optical depth may exceed unity (e.g., around $\lambda_0 = 100\text{--}200 \mu\text{m}$ for dusty star-forming galaxies; [Casey 2012](#)).

It is important to take into account the cosmic microwave background (CMB) effect, especially in the high- z universe since the CMB temperature increases with redshift as $T_{\text{CMB},z} = T_{\text{CMB},z=0} \times (1+z)$. The CMB affects the T_{dust} measurements in two ways: (1) additional heating source of dust grains within galaxies and (2) background radiation against which we observe the submillimeter fluxes from galaxies ([da Cunha et al. 2013](#)). After considering these effects following [da Cunha et al. \(2013\)](#), Equation (4) becomes

$$F_{\nu_{\text{obs}}} = \left(\frac{1+z}{d_L^2} \right) \left(\frac{1 - e^{-\tau_\nu}}{\tau_\nu} \right) M_d \kappa_\nu [B_\nu(T_{\text{dust}}) - B_\nu(T_{\text{CMB}})]. \quad (5)$$

In the optically thin limit ($\nu_0 \rightarrow \infty$, $\lambda_0 \rightarrow 0$, and thus $\tau_\nu \ll 1$), the term representing the effect of the optical depth $(1 - e^{-\tau_\nu}/\tau_\nu)$ is asymptotically unity. Therefore the formula of the optically thin MBB becomes

$$F_{\nu_{\text{obs}}} = \left(\frac{1+z}{d_L^2} \right) M_d \kappa_\nu [B_\nu(T_{\text{dust}}) - B_\nu(T_{\text{CMB}})]. \quad (6)$$

In this work, we use Equation (6) to estimate T_{dust} , β_{dust} , and M_{dust} in the same manner as previous studies (e.g., [Dudzevičiūtė et al. 2020](#); [Bakx et al. 2021](#); [da Cunha et al. 2021](#); [Algera et al. 2023](#)). We note that the resulting L_{IR} does not change under the assumption of the optically thick MBB with $\lambda_0 = 100 \mu\text{m}$, whereas T_{dust} becomes higher than those with the optically thin assumption.

We use the Markov Chain Monte Carlo (MCMC) algorithm to fit the MBB profiles by utilizing the EMCEE library. The fitting results are shown in Figure 5. We adopt a logarithmically uniform prior on the dust masses and dust temperatures with a range of $\log_{10}(M_{\text{dust}}/M_{\odot}) \in [4, 10]$ and $T_{\text{dust}}/\text{K} \in [T_{\text{CMB},z}, 120]$, respectively. Note that there is no significant impact on our conclusion if we change the upper edge of the prior distribution of T_{dust} to 150 K. Since the sampling range of the FIR SED is not enough to constrain β_{dust} , we adopt a Gaussian prior with a mean value of $\langle \beta_{\text{dust}} \rangle = 1.8$ and a standard deviation of $\sigma_{\beta_{\text{dust}}} = 0.5$ to take the β_{dust} uncertainties into account to those of T_{dust} , M_{dust} , and the resulting L_{IR} . This value is consistent with that of the Milky Way (Planck Collaboration et al. 2014), the local galaxies (Cortese et al. 2014; Lamperti et al. 2019), local ULIRG (Clements et al. 2018), and high- z galaxies (da Cunha et al. 2021; Witstok et al. 2023). The results do not strongly depend on the prior distribution of β_{dust} as there is no significant difference if we apply a uniform prior of $\beta_{\text{dust}} \in [1.5, 2.5]$.²² We fit the optically thin MBB model to the measured flux densities. In the case that the measured ALMA fluxes in any bands are upper limit, we adopt the methodology described in Sawicki (2012), which accounts for the Gaussian noise distribution of the probability distribution. In a nutshell, the probability of a model flux S_{model} can be calculated by integrating a Gaussian distribution, which has a center of S_{model} and dispersion of $\sigma_{S_{\text{model}}}$, from negative infinity to the 3σ value of the upper limits. For instance, the probabilities taking model fluxes of $S_{\text{model}} = S_{1\sigma}$ or $S_{3\sigma}$ are penalized by $\sim 0.1\%$ or $\sim 50\%$, respectively. Therefore the model fluxes above 3σ are not forbidden but the model fluxes much smaller than 3σ are preferred. This is a reason why the resulting MBB sometimes yields model fluxes above the 3σ upper limit (see Figure 5). We compute best-fit values and 1σ uncertainties from the modes with the highest posterior density intervals.

Figure 5 shows the results of the MBB fittings for the SERENADE galaxies. Our MBB fitting successfully constrains T_{dust} , M_{dust} , and L_{IR} , while some galaxies such as J020038-021052 or J0235+0532 need observations at shorter wavelengths or deeper observations are necessary to obtain more robust constraints on the parameters. The fitting results are summarized in Table 2.

We compare the derived infrared luminosities (L_{IR} ; 8–1000 μm) of the SERENADE galaxies with the literature in Figure 6. For a fair comparison with the galaxies previously reported, we conduct the same flux measurements and MBB fittings for the galaxies at $5 < z < 8$ in the literature. While our target galaxies were originally selected by their bright UV emission, the L_{IR} of the SERENADE galaxies spans a wide range, specifically from $\log L_{\text{IR}}[L_{\odot}] \sim 11.5$ comparable to normal galaxies at $z \sim 7$ (e.g., Ferrara et al. 2022) to $\log L_{\text{IR}}[L_{\odot}] \sim 13.0$ similar to dusty starburst galaxies (e.g., Riechers et al. 2013).

4. Results

4.1. β_{UV} versus IRX Relationship

In Figure 7, we plot the IRX– β_{UV} diagram of the SERENADE galaxies. The results for the individually detected galaxies include uncertainties of the FIR SED. Meanwhile, the upper limits of the undetected galaxies are calculated by

²² In the case of the uniform prior, the fitting results tend to prefer slightly lower β_{dust} and T_{dust} values compared with those under the Gaussian prior.

assuming $T_{\text{dust}} = 45$ K (a representative T_{dust} of SERENADE galaxies). We find that our result from the stacking analysis supports a shallower IRX– β_{UV} relation than the Calzetti (Calzetti et al. 2000) and Meurer (Meurer et al. 1999) relations. Furthermore, our results prefer a shallower relation than the SMC extinction (e.g., Pettini et al. 1998; Gordon et al. 2003; Reddy et al. 2018) regardless of the intrinsic UV slope ($\beta_{\text{UV,int}} = -2.23$ or -2.62). Such a shallow relation matches well the relation reported in Fudamoto et al. (2020a) with $\beta_{\text{UV,int}} = -2.62$. This shallower relation aligns with the findings of Reddy et al. (2018) and Faisst et al. (2017). Reddy et al. (2018) expect that galaxies with lower stellar metallicities at high redshift ($Z_* \sim 0.14Z_{\odot}$) favor a shallow IRX– β_{UV} relation with bluer intrinsic UV slope $\beta_{\text{UV,int}} = -2.62$. Faisst et al. (2017) suggest the Charlot & Fall (2000) model with optically thin cloud composed of the SMC-like dust explains the trend that young, metal-/dust-poor galaxies in the early Universe may tend to locate to a lower part of the IRX– β_{UV} diagram. Since our targeted luminous LBGs at $z \sim 6$ are expected to have subsolar stellar metallicities, such as $\sim 0.4Z_{\odot}$ as presented in Harikane et al. (2020a), our results have a good agreement with the prediction in Reddy et al. (2018). As discussed in Bowler et al. (2024), the difference from the results at $z \sim 5-7$ (Fudamoto et al. 2020a; Bowler et al. 2024) at $\beta_{\text{UV}} = [-3; -1]$ mainly comes from the difference in T_{dust} . Our estimate of $T_{\text{dust}} \sim 25$ K for the stacking sample with $\beta_{\text{UV}} = [-3; -1]$ from multiband observations is lower by ~ 20 K than the assumptions in these studies, and it leads to ~ 0.7 dex offset in the IRX.

We test potential biases in sample selection with the same procedure in Section 3.4 and find that the result remains consistent even when selecting galaxies only from the SHELLQs survey. Some studies have implied that the methodology for estimating β_{UV} could systematically change the IRX– β_{UV} relation. For instance, Álvarez-Márquez et al. (2019) suggested that the β_{UV} estimated by power-law fitting ($\beta_{\text{UV,power}}$) may be biased to redder values by $\Delta\beta_{\text{UV}} \sim 0.35$ than that derived by SED fitting ($\beta_{\text{UV,SED}}$). Furthermore, Reddy et al. (2015) demonstrated that β_{UV} calculated within the rest-frame wavelength range of $\lambda_{\text{rest}} = 1260-1750$ Å ($\beta_{\text{UV,narrow}}$) might be redder than that within the range of $\lambda_{\text{rest}} = 1260-2600$ Å ($\beta_{\text{UV,wide}}$) especially in the spectrum with large β_{UV} . Given the analysis in Reddy et al. (2015), the redder β_{UV} bin of our galaxies, spanning $-0.5 \lesssim \beta_{\text{UV}} \lesssim 0.5$, may intrinsically be bluer than the current estimation such as $\beta_{\text{UV}} \sim -0.8$ since four of five galaxies within $-0.5 \lesssim \beta_{\text{UV}} \lesssim 0.5$ have limited wavelength coverages of $\lambda_{\text{rest}} = 1260-1700$ Å. However, even after changing $\beta_{\text{UV}} \sim 0.0$ to -0.8 , our results still favor a shallow IRX– β_{UV} relation such as $z \sim 5.5$ results from Fudamoto et al. (2020a). To secure robust measurements of UV slopes, NIR observations that cover the rest-frame optical wavelengths at $z \sim 6$ are imperative.

4.2. SFR Density at $z \sim 6$

As our observations are follow-up observations of UV-bright galaxies, we estimate the dust-obscured star formation activities of the UV-selected galaxies at $z \sim 6$. The focus of this paper, the contribution of dust-obscured star formation in the UV-selected galaxies, is complementary to the studies based on the IR-based source identification (e.g., Gruppioni et al. 2020; Zavala et al. 2021; Fujimoto et al. 2023) to comprehensively understand the dust-obscured star formation. Our starting point

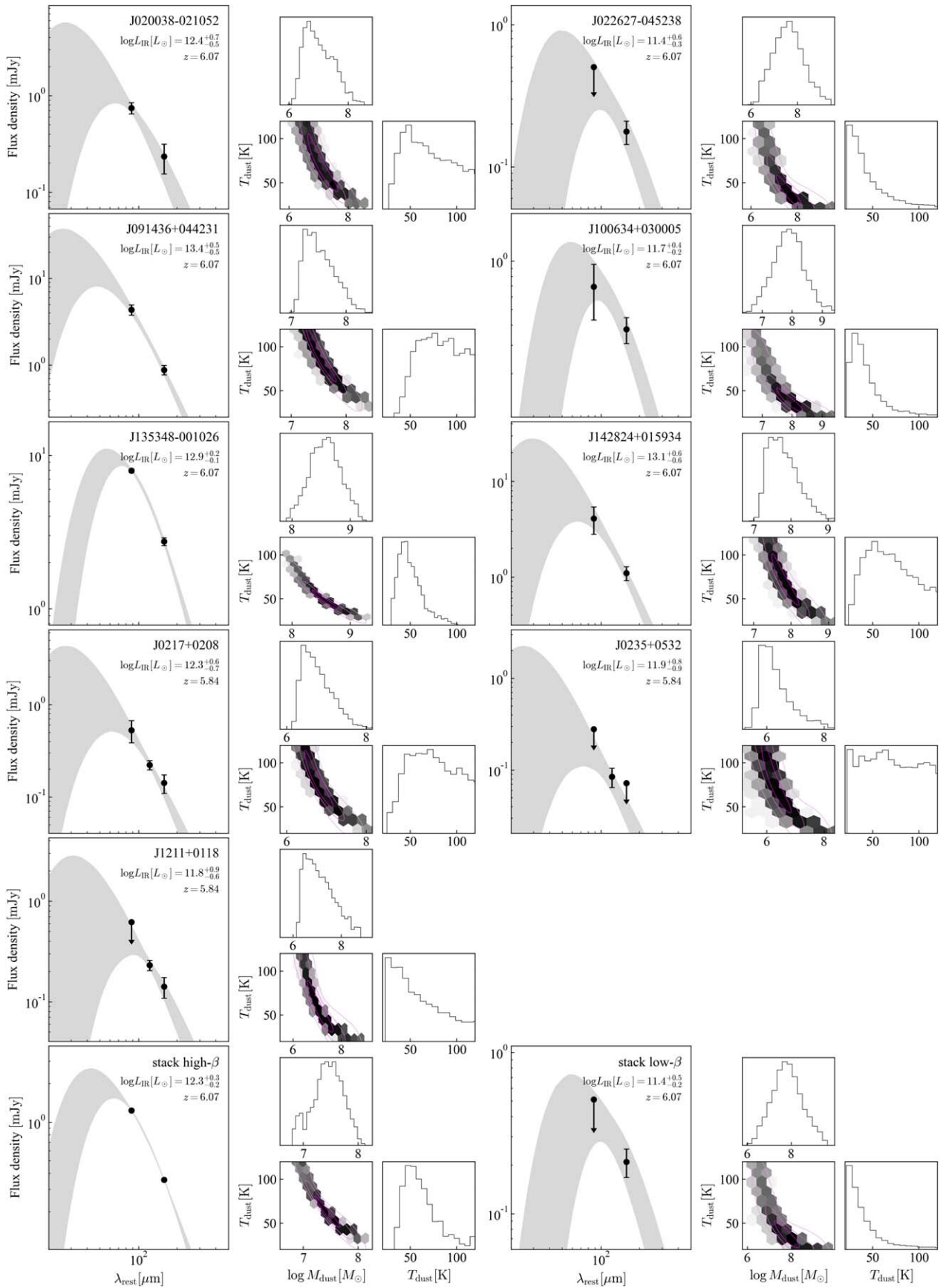


Figure 5. Optically thin MBB fitting results of the SERENADE galaxies. The left panels show the 1σ confidence interval of the MBB profiles as a function of the rest-frame wavelength (shaded area). The observed fluxes and 3σ upper limits are shown by the black-filled circles. The right panels illustrate the posterior distributions of the MCMC procedure with 1σ , 2σ , and 3σ contours. The best fit and 1σ uncertainties of L_{IR} are shown inside the left panels.

Table 2
Summary of the Parameters Related to Rest-frame FIR Emission

ID	$S_{158 \mu\text{m}}$ (mJy)	$S_{88 \mu\text{m}}$ (mJy)	$S_{205 \mu\text{m}}$ (mJy)	$S_{122 \mu\text{m}}$ (mJy)	$S_{110 \mu\text{m}}$ (mJy)	$S_{52 \mu\text{m}}^a$ (mJy)	T_{dust}^b (K)	$\log L_{\text{IR}}$ (L_{\odot})	$\log M_{\text{dust}}$ (M_{\odot})
SERENADE									
J020038-021052	0.24 ± 0.08	0.75 ± 0.10	$56.4^{+28.7}_{-24.1}$	$11.9^{+0.7}_{-0.2}$	$6.8^{+0.6}_{-0.3}$
J021033-052304	...	1.93 ± 0.25	(45)	$12.3^{+0.1}_{-0.1}$	$9.0^{+0.1}_{-0.1}$
J021041-055917	≤ 0.14	(45)	≤ 11.6	≤ 7.3
J021244-015824	≤ 0.17	≤ 0.62	(45)	≤ 11.7	≤ 7.4
J021735-051032	≤ 0.07	(45)	≤ 11.3	≤ 7.0
J021807-045841	≤ 0.06	(45)	≤ 11.2	≤ 6.9
J021838-050943	≤ 0.06	(45)	≤ 11.2	≤ 7.0
J022023-050431	≤ 0.16	≤ 0.83	(45)	≤ 11.7	≤ 7.4
J022627-045238	0.18 ± 0.03	≤ 0.50	$27.4^{+20.3}_{-7.6}$	$11.2^{+0.5}_{-0.2}$	$7.6^{+0.7}_{-0.6}$
J024801-033258	≤ 0.03	(45)	≤ 11.0	≤ 6.7
J045408-030014	≤ 0.11	≤ 0.26	(45)	≤ 11.5	≤ 7.2
J085723+014254	≤ 0.13	≤ 0.33	(45)	≤ 11.5	≤ 7.2
J091436+044231	0.88 ± 0.11	4.35 ± 0.59	$75.6^{+24.4}_{-23.8}$	$13.4^{+0.2}_{-0.6}$	$7.4^{+0.3}_{-0.1}$
J100008+021136	≤ 0.04	(45)	≤ 11.1	≤ 6.8
J100634+030005	0.38 ± 0.07	0.69 ± 0.26	$30.1^{+16.9}_{-7.8}$	$11.6^{+0.3}_{-0.2}$	$7.9^{+0.6}_{-0.5}$
J114412-000613	≤ 0.13	≤ 0.46	(45)	≤ 11.6	≤ 7.3
J135348-001026	2.74 ± 0.16	7.97 ± 0.23	$44.1^{+16.9}_{-10.5}$	$12.9^{+0.2}_{-0.1}$	$8.6^{+0.3}_{-0.4}$
J142824+015934	1.10 ± 0.18	4.10 ± 1.30	$49.3^{+37.0}_{-14.8}$	$12.9^{+0.6}_{-0.4}$	$7.6^{+0.5}_{-0.2}$
SERENADE pilot (Harikane et al. 2020b)									
J1211+0118	0.14 ± 0.03	≤ 0.62	...	0.23 ± 0.03	$37.3^{+36.1}_{-13.5}$	$11.3^{+0.9}_{-0.2}$	$6.7^{+0.8}_{-0.2}$
J0217+0208	0.14 ± 0.03	0.53 ± 0.14	...	0.22 ± 0.03	$56.8^{+36.0}_{-18.9}$	$12.4^{+0.4}_{-0.7}$	$6.6^{+0.5}_{-0.1}$
J0235+0532	≤ 0.07	≤ 0.28	...	0.09 ± 0.02	$53.2^{+43.7}_{-21.0}$	$11.9^{+1.1}_{-0.3}$	$6.1^{+0.6}_{-0.3}$
$z \sim 7$ LBGs (Hashimoto et al. 2019; Bakx et al. 2021; Akins et al. 2022; Witstok et al. 2022; Algera et al. 2023)									
COS-2987030247	≤ 0.02	≤ 0.19	(45)	≤ 10.9	≤ 6.6
COS-3018555981	0.05 ± 0.01	≤ 0.20	$30.1^{+23.7}_{-7.3}$	$10.9^{+0.5}_{-0.2}$	$7.0^{+0.7}_{-0.5}$
UVISTA-Z-001	0.07 ± 0.01	0.23 ± 0.07	$31.4^{+35.2}_{-9.1}$	$11.3^{+0.7}_{-0.3}$	$6.7^{+0.9}_{-0.5}$
UVISTA-Z-007	≤ 0.05	≤ 0.30	(45)	≤ 11.3	≤ 7.0
UVISTA-Z-019	0.07 ± 0.01	≤ 0.83	$32.5^{+52.8}_{-9.9}$	$12.2^{+0.2}_{-1.4}$	$6.5^{+0.6}_{-0.2}$
A1689-zD1	1.09 ± 0.17	2.68 ± 0.19	2.04 ± 0.14	1.84 ± 0.43	$45.3^{+8.5}_{-6.6}$	$11.4^{+0.1}_{-0.1}$	$7.1^{+0.2}_{-0.2}$
B14-65666	0.13 ± 0.03	0.47 ± 0.14	0.22 ± 0.01	...	$51.3^{+33.8}_{-23.1}$	$11.8^{+0.7}_{-0.5}$	$6.7^{+0.6}_{-0.2}$
REBELS-12	0.05 ± 0.01	≤ 0.32	$34.9^{+47.8}_{-11.3}$	$11.1^{+1.0}_{-0.2}$	$6.3^{+0.7}_{-0.3}$
REBELS-25	0.22 ± 0.01	0.69 ± 0.03	$41.2^{+20.2}_{-9.0}$	$11.9^{+0.2}_{-0.1}$	$7.5^{+0.4}_{-0.3}$
REBELS-38	0.18 ± 0.02	0.51 ± 0.10	$43.6^{+19.4}_{-14.2}$	$11.7^{+0.4}_{-0.2}$	$7.4^{+0.3}_{-0.5}$
$z \sim 5.5$ LBGs (Faisst et al. 2020b)									
HZ4	0.27 ± 0.03	...	0.11 ± 0.01	...	0.50 ± 0.07	...	$47.9^{+35.4}_{-14.3}$	$12.0^{+0.6}_{-0.3}$	$6.9^{+0.4}_{-0.3}$
HZ6	0.42 ± 0.04	...	0.27 ± 0.04	...	0.58 ± 0.09	...	$25.7^{+7.6}_{-7.8}$	$11.4^{+0.2}_{-0.1}$	$8.3^{+0.5}_{-0.5}$
HZ9	0.59 ± 0.09	...	0.31 ± 0.02	...	1.18 ± 0.09	...	$42.5^{+29.4}_{-11.5}$	$12.1^{+0.5}_{-0.2}$	$7.5^{+0.4}_{-0.3}$
HZ10	1.87 ± 0.08	...	0.69 ± 0.03	...	3.39 ± 0.18	...	$33.4^{+10.0}_{-5.4}$	$12.5^{+0.2}_{-0.1}$	$8.6^{+0.2}_{-0.4}$
Stack									
$-3 < \beta_{\text{UV}} < -1$	0.21 ± 0.04	≤ 0.63	$50.4^{+24.6}_{-9.5}$	$12.2^{+0.7}_{-0.2}$	$7.4^{+0.3}_{-0.2}$
$-1 \leq \beta_{\text{UV}} < 1$	0.36 ± 0.01	1.24 ± 0.03	$26.0^{+14.5}_{-6.5}$	$11.3^{+0.4}_{-0.2}$	$7.8^{+0.7}_{-0.6}$

Note.

^a Dust continuum fluxes at each wavelength. For cases with nondetection, 3σ upper limits are shown.

^b For the galaxies whose dust temperatures are not constrained due to insufficient observations or nondetections, we assume the representative dust temperature of the SERENADE galaxies ($T_{\text{dust}} = 45$ K).

is the galaxy UV luminosity function presented in Harikane et al. (2022). The selection criteria adopted in their study allow the identification of not only blue i -dropout LBGs but also those with moderately red colors encompassing a β_{UV} range of $-3 \leq \beta_{\text{UV}} \leq 1$. We convert the UV luminosities of the galaxies into IR luminosities in each UV absolute magnitude bin by utilizing both the $M_{\text{UV}}-\beta_{\text{UV}}$ relation including fainter galaxies in the literature and the $\text{IRX}-\beta_{\text{UV}}$ relation. Specifically, we adopt the broken linear relationship with a combination of

Equation (2) at $M_{\text{UV}} \lesssim -22$ mag and Equation (1) at $M_{\text{UV}} \gtrsim -22$ mag for the $M_{\text{UV}}-\beta_{\text{UV}}$ relation (Figure 2). We fit a linear function as parameterized in Equation (2) to smoothly connect to the linear function in Equation (1). For the $\text{IRX}-\beta_{\text{UV}}$ relation, we apply the extinction curve reported in Fudamoto et al. (2020a) as a fiducial one due to its alignment with our measurements (Figure 7). We estimate uncertainties using bootstrap techniques, ensuring the propagation of uncertainties in each relationship. Subsequently, we derive the UV-based

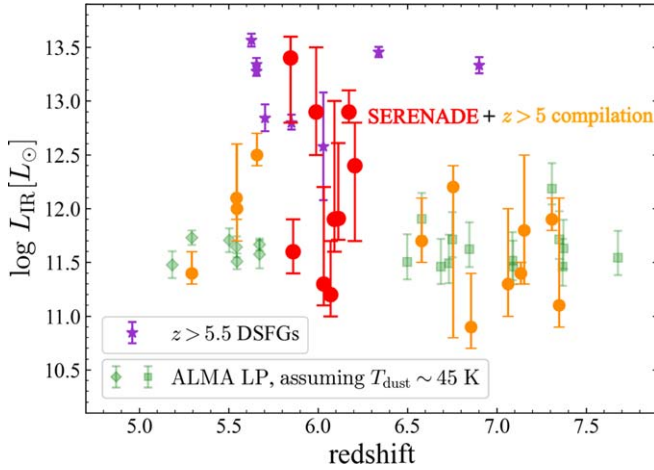


Figure 6. IR luminosities of the SERENADE galaxies (red) and those at $5 < z < 8$ in the literature (orange) as a function of the redshift. We compare the results with galaxies reported in the ALMA large programs in which fixed dust temperatures are assumed (green symbols; Faist et al. 2020b; Inami et al. 2022) and DSFGs at $z > 5.5$ (purple stars; Riechers et al. 2013; Marrone et al. 2018; Zavala et al. 2018; Casey et al. 2019; Reuter et al. 2020). The definition of L_{IR} is uniform except for the HFLS3 at $z = 6.34$ (L_{FIR} , 42.5–122.5 μm ; Riechers et al. 2013).

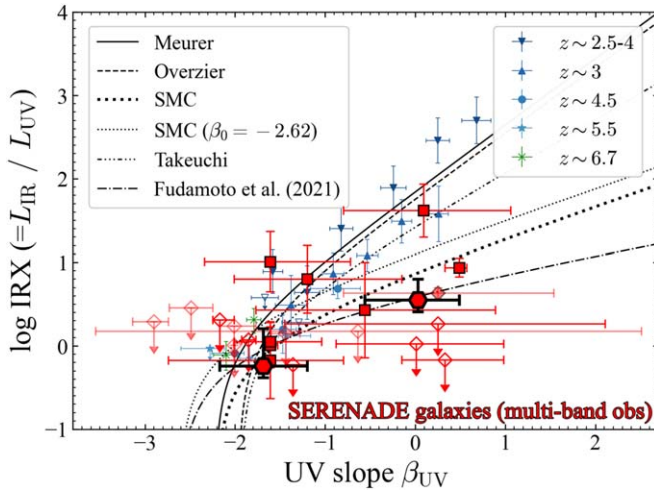


Figure 7. IRX– β_{UV} relation. The filled red squares are the individual galaxies whose dust temperatures are constrained with multiband observations. The filled pentagons show the results of the stacking analysis. The filled and open diamonds are galaxies whose dust temperatures are not constrained due to insufficient observations or nondetections. For these cases, we assume the dust temperature of 45 K. For the stacking analysis, we use the galaxies observed in both ALMA bands. The blue and green markers represent the previous measurements of the galaxies at $z = 2.5\text{--}4$ (Fudamoto et al. 2020b), $z \sim 3$ (Álvarez-Márquez et al. 2019), $z \sim 4.5$ and $z \sim 5.5$ (Fudamoto et al. 2020a), and $z \sim 6.7$ (Bowler et al. 2024). The best-fit relations from local (Prevot et al. 1984; Meurer et al. 1999; Calzetti et al. 2000; Gordon et al. 2003; Overzier et al. 2011; Takeuchi et al. 2012) and high- z galaxies (e.g., Álvarez-Márquez et al. 2016; Reddy et al. 2018; Fudamoto et al. 2020a) are also plotted.

SFR from the UV luminosities and IR-based SFR from IR luminosities converted above following the conversion factors in Madau & Dickinson (2014) with a Chabrier (2003) initial mass function (IMF),

$$\text{SFR}_{\text{UV}} = 0.76 \times 10^{-28} L_{\text{UV}} (\text{erg s}^{-1} \text{Hz}^{-1}), \quad (7)$$

$$\text{SFR}_{\text{IR}} = 2.64 \times 10^{-44} L_{\text{IR}} (\text{erg s}^{-1}), \quad (8)$$

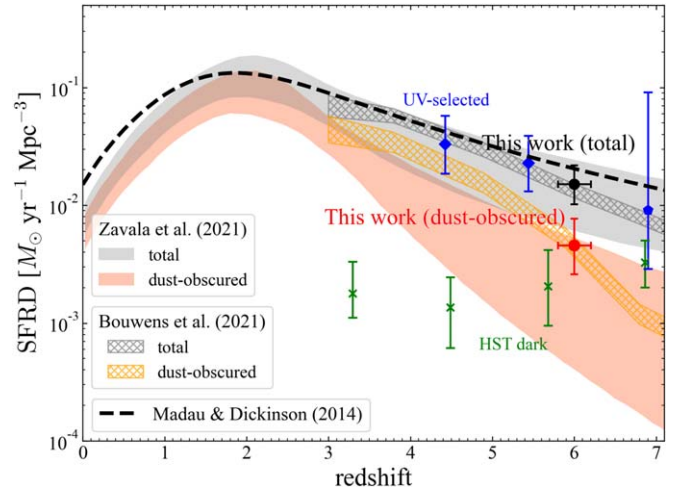


Figure 8. Cosmic SFRD as a function of redshift. The black- and red-filled circles indicate our results of the total and dust-obscured SFRDs, respectively, based on the IRX– β_{UV} relations consistent with our results and the $M_{\text{UV}}\text{--}\beta_{\text{UV}}$ relation constrained with our galaxies and the fainter galaxies in B14. Previous studies are represented in the shaded areas for both the dust-obscured and unobscured SFRDs (Bouwens et al. 2021; Zavala et al. 2021). The total SFRD presented in Madau & Dickinson (2014) is shown by the black-dashed line. The dust-obscured SFRD of the UV-selected galaxies from the ALPINE and REBELS survey are shown by blue diamonds and pentagons (Khusanova et al. 2021; Algera et al. 2023; see also Fudamoto et al. 2020a; Gruppioni et al. 2020; Inami et al. 2022). The contribution of the HST-dark galaxies to the SFRD are also shown by the green crosses (Barrufet et al. 2023b). Our results suggest that the dust-obscured star formation activity of LBGs does not significantly contribute to the total SFR, $\sim 30\%$ at $z \sim 6$.

and obtain the number densities of the galaxies as a function of their total SFR. We then integrate the SFR function with a range from $M_{\text{UV}} = -17$ mag following previous studies (e.g., Bouwens et al. 2012, 2021).

Figure 8 shows the SFRD as a function of redshift. Our total and dust-obscured SFRD estimates are represented in the black- and red-filled circles, respectively. Our analyses indicate that the dust-obscured star formation in UV-selected galaxies contributes $31^{+8}_{-8}\%$ to the total star formation at $z \sim 6$. This contribution is slightly larger than that predicted in Bouwens et al. (2021), $\sim 24\%$. The reason for this discrepancy comes from our adoption of the Fudamoto et al. (2020a) IRX– β_{UV} relation, which is a shallower IRX but smaller intrinsic β_{UV} of -2.62 than the Meurer relation used in Bouwens et al. (2021). Our estimation of the contribution of the dust-obscured star formation is near the upper bound of the results in Zavala et al. (2021) while their study focuses on dusty galaxies identified with ALMA.

For a further comparison, we also calculate the SFRD with the different combinations of the $M_{\text{UV}}\text{--}\beta_{\text{UV}}$ and IRX– β_{UV} relations. We test the following two cases with bluer UV slopes than our fiducial estimate above to consider the possibility that the UV slope is overestimated as discussed in Section 4.1: (1) linear $M_{\text{UV}}\text{--}\beta_{\text{UV}}$ and SMC IRX– β_{UV} relations (2) linear $M_{\text{UV}}\text{--}\beta_{\text{UV}}$ and Calzetti IRX– β_{UV} relations. Here, linear $M_{\text{UV}}\text{--}\beta_{\text{UV}}$ suggests the extrapolated linear relation parameterized in B14. The calculated SFRDs are listed in Table 3. We find that the IRX– β_{UV} relation has a more profound impact on the resulting SFRD than the $M_{\text{UV}}\text{--}\beta_{\text{UV}}$ relation, but the maximum contribution of the dust-obscured star formation is $\sim 45\%$ even with aggressive dust correction assumptions of (2), which is not preferred from the IRX measurements in this

Table 3
Estimated SFRD under Different Assumptions

Assumption		Total	Dust Obscured
$M_{UV-\beta_{UV}} + IRX-\beta_{UV}$		$(M_{\odot} \text{ yr}^{-1} \text{ Mpc}^{-3})$	
B14+This work	Fudamoto et al. (2020a)	$-1.82^{+0.17}_{-0.17}$	$-2.33^{+0.23}_{-0.25}$
B14 extrapolation	SMC	$-1.72^{+0.18}_{-0.17}$	$-2.06^{+0.24}_{-0.27}$
B14 extrapolation	Meurer	$-1.73^{+0.23}_{-0.22}$	$-2.13^{+0.37}_{-0.50}$
$M_{UV-f_{obs}}$		$(M_{\odot} \text{ yr}^{-1} \text{ Mpc}^{-3})$	
This work		$-1.90^{+0.19}_{-0.17}$	$-2.72^{+0.40}_{-0.41}$

study. Thus, we conclude that the contribution of the dust-obscured star formation activity from LBGs is not dominant and the assumption of the dust correction does not strongly change the total SFRD at $z \sim 6$. Note that our estimations of the dust-obscured star formation miss very dusty galaxies such as submillimeter galaxies (e.g., Dudzevičiūtė et al. 2020) or HST-dark galaxies (Wang et al. 2019) given our focus on the UV-bright galaxies. A recent JWST investigation on HST-dark galaxies implies an almost constant contribution of the dust-obscured star formation activity from faint dusty galaxies from $z=4$ to $z=7$ (Barrufet et al. 2023b), although their contributions are predicted to be comparable with that of our estimation at $z \sim 6$.

4.3. Obscured Fraction of the Star Formation

Apart from using the $M_{UV-\beta_{UV}}$ and $IRX-\beta_{UV}$ relationships, the dust-obscured star formation in LBGs can be estimated through the direct compilation of the obscured fraction of the star formation, presented as a function of either stellar mass or absolute UV magnitude ($f_{obs}-M_{UV}$ or $f_{obs}-M_{*}$). The obscured fraction is defined by the ratio of the obscured SFR (SFR_{IR}) to the total (UV+IR) SFR (SFR_{UV+IR}). The dust-obscured SFRD is directly derived via the UV luminosity function and $f_{obs}-M_{UV}$ relation in a similar way to that via the stellar mass function and $f_{obs}-M_{*}$ relation utilized in some previous studies (e.g., Algera et al. 2023).

To investigate the $f_{obs}-M_{UV}$ relation for the SERENADE galaxies, we split the sample into three distinct M_{UV} bins, $M_{UV} = [-24.5, -23.5]$, $[-23.5, -22.0]$, and $[-22.0, -20.5]$. Owing to the limited observation in $88 \mu\text{m}$ within the $M_{UV} = [-22.0, -20.5]$ range, we conduct the stacking analysis for just the rest-frame $158 \mu\text{m}$, rather than limiting the sample to the galaxies observed in both Band 6 and Band 8. Following the methodologies in Sections 3.4 and 3.3, we estimate stacked dust continuum fluxes and convert them to L_{IR} assuming an optically thin MBB profile with $T_{dust} = 45 \text{ K}$ and $\beta_{dust} = 1.8$ to perform a fair comparison with the previous results (Fudamoto et al. 2020a; Algera et al. 2023). Then we calculate f_{obs} by translating the inferred L_{IR} into SFR_{IR} and the average L_{UV} of the bin into SFR_{UV} . We also calculate individual f_{obs} for reference.

Figure 9 shows the derived individual and stacked f_{obs} values in red markers. The best-fit $f_{obs}-M_{UV}$ relation and 1σ uncertainties estimated by bootstrap are also shown by the red solid line and shaded area. Given that previous studies at $z \sim 4.5, 5.5,$ and 7 have measured the f_{obs} relative to the stellar mass, we convert them to M_{UV} based on the scaling relations in Song et al. (2016). We note that the conversion is just for

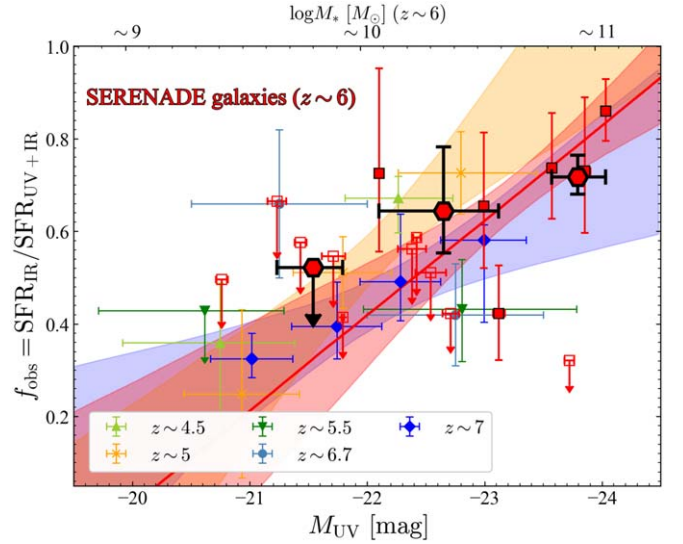


Figure 9. Obscured fraction of the star formation against the absolute UV magnitude ($M_{UV}-f_{obs}$). Our individual measurements of the galaxies detected and undetected in the dust continuum are shown by the red-filled and open squares, respectively. We also show the best fit and 1σ uncertainty of $M_{UV}-f_{obs}$ relation (red solid line and shaded region) derived from the stacked results (red-filled pentagons). We convert M_{*} into M_{UV} using the scaling relation in Song et al. (2016) for previous results for a direct comparison with our results. The stellar mass converted from M_{UV} at $z \sim 6$ is also shown in the x-axis for reference. The light green, orange, and green symbols are the results at $z \sim 4.5, 5,$ and 5.5 (Fudamoto et al. 2020a; I. Mitsuhashi et al. 2024, in preparation). The blue and cyan symbols are the results at $z \sim 6.7$ and $z \sim 7$ from Bowler et al. (2024) and Algera et al. (2023), respectively.

reference given the large uncertainties in the star formation histories of high- z galaxies (e.g., Tacchella et al. 2022; Stiavelli et al. 2023; Looser et al. 2024). Our results show a good agreement in the range of $M_{UV} \geq -23.1$ with the previous result at $z \sim 5$, and add a constraint within the range of $M_{UV} = [-24.5, -23.5]$ corresponding to $M_{*} \sim 10^{11} M_{\odot}$. Our best-fit relation at $z \sim 6$ shows a positive trend between the UV brightness and f_{obs} . This is similar to the previous results showing positive trends with $M_{*}-f_{obs}$ at $z \sim 4.5, z \sim 5,$ and $z \sim 7$ from ALPINE, CRISTAL, and REBELS survey (Fudamoto et al. 2020a; Algera et al. 2023; I. Mitsuhashi et al. 2024, in preparation). Our results show slightly higher f_{obs} than that of ALPINE galaxies at $z \sim 5.5$ (Fudamoto et al. 2020a) at the range of $\log M_{*}[M_{\odot}] = 10-11.1$ corresponding $M_{UV} = [-23.5, -22.0]$. Selecting targets on the basis of Ly α emission might induce a bias toward dust-poor galaxies, and result in the slightly lower f_{obs} in Fudamoto et al. (2020a). While a significant population (90%) of the ALPINE galaxies within $\log M_{*}[M_{\odot}] = 10-11.1$ are identified by Ly α emission (Faisst et al. 2020b), only 50% of the SERENADE galaxies show Ly α emission. Bowler et al. (2024) suggest the anticorrelation between M_{UV} and f_{obs} at $z \sim 6.7$, which is contrary to the other results at $z > 4$. As described in Section 3.2, the effect of scatter in the obscuration or geometry of their target galaxies may be one of the causes of this difference.

Based on the estimated $M_{UV}-f_{obs}$ relation and the UV luminosity function presented in Harikane et al. (2022), we calculate the total and dust-obscured SFRD, following Section 4.2. The calculated SFRDs are shown in Table 3,

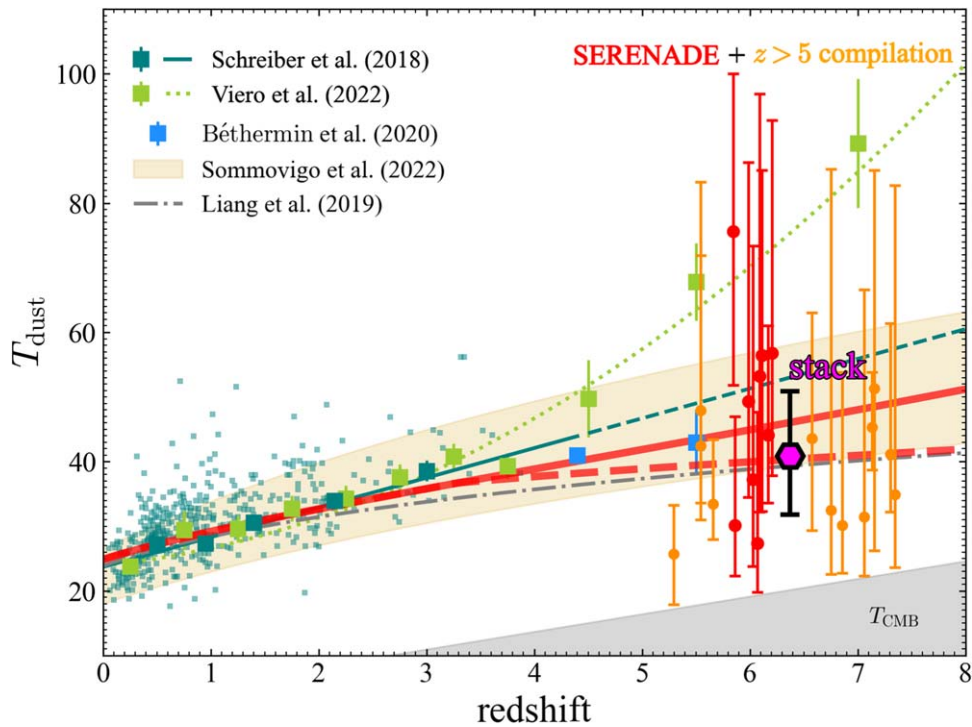


Figure 10. Dust temperature as a function of the redshift. Individual results of the SERENADE galaxies are shown by the red-filled circles and our measurements for the $z \gtrsim 5$ galaxies in the literature are shown by the orange markers (Hashimoto et al. 2019; Laporte et al. 2019; Bakx et al. 2020, 2021; Faisst et al. 2020a; Sugahara et al. 2021; Witstok et al. 2022; Algera et al. 2024). The magenta pentagon shows the stacked results of the galaxies at $z \sim 6-7$. For comparison, previous results based on the stacking analysis and the expected redshift evolution are shown by the blue, light blue, and green colors (Schreiber et al. 2018; Béthermin et al. 2020; Viero et al. 2022). The model prediction of the redshift evolution from Liang et al. (2019) is shown as the gray line and the yellow-shaded region indicates the model from Sommovigo et al. (2022) with the range of $Z \sim Z_{\odot}$ and $N_{\text{H}} \sim 10^{20} \text{ cm}^{-2}$. The red lines represent the T_{dust} evolution calculated based on the analytical model of Sommovigo et al. (2022) and observed redshift evolution of t_{gas} (Tacconi et al. 2020) and Z (Sanders et al. 2021) under the assumption of continuous (solid) and no (dashed) M_{*} - Z evolution at $z > 3.3$. The calculated T_{dust} evolution explains our result as well as the results at $z \lesssim 5$.

corroborating the limited contribution of the dust-obscured star formation activity from LBGs ($\sim 15\%$) as shown in Section 4.2.

4.4. T_{dust} Evolution

In Figure 10, we plot T_{dust} as a function of the redshift. Among 28 galaxies covered in the multiband observations, we plot 21 galaxies that are individually detected in Band 6 and/or Band 8, allowing us to measure T_{dust} . To estimate average T_{dust} at $z \sim 6-7$, we also perform the stacking analysis of the galaxies observed in both $88 \mu\text{m}$ and $158 \mu\text{m}$. From the 28 galaxies, we exclude four $z \sim 5.5$ galaxies due to the different rest-frame wavelength coverage and two $z \sim 6$ galaxies as in Section 3.4, resulting in a total of 22 galaxies for the stacking analysis. We conduct an average stack and estimate T_{dust} and its uncertainty from MBB fitting with the Gaussian β_{dust} prior as described in Section 3.5. There is no major difference in the resulting T_{dust} when we use median stacking instead of average stacking. Individual measurements from SERENADE (red-filled circles) and an additional $5 < z < 8$ galaxies from the literature (orange-filled circles) are shown, along with the stacked result (magenta hexagon). The stacked result suggests that an average dust temperature is $T_{\text{dust}} = 40.9^{+10.0}_{-9.1}$ K. Our results support the linear relation of $\propto(1+z)^1$ (Schreiber et al. 2018) rather than the quadratic relation $\propto(1+z)^2$ (Viero et al. 2022). The individual measurements have a large scatter of $\Delta T_{\text{dust}} \sim 12$ K at $z = 5-8$ (see also Hashimoto et al. 2019; Laporte et al. 2019; Bakx et al. 2020, 2021; Faisst et al. 2020a; Sugahara et al. 2021; Witstok et al. 2022; Algera et al. 2024).

5. Discussion of T_{dust} Evolution

As shown in the previous section, our result of $T_{\text{dust}} \sim 40$ K supports a mild increase in T_{dust} as a function of redshift. The theoretical predictions from Liang et al. (2019) also support our result, where they expect an increase in the specific star formation rate (sSFR) may result in an increasing trend of T_{dust} against the redshift. Our result matches the evolution trend presented in Sommovigo et al. (2022) with a gas column density of $\log N_{\text{H}} [\text{cm}^{-2}] \sim 20$ under the optically thin assumption, where they predict that an increasing trend of T_{dust} against redshift associates with a higher SFR or a shorter gas depletion timescale (t_{gas}) at high- z (see also Vallini et al. 2024).

To better understand the increasing trend of T_{dust} , we calculate the T_{dust} evolution by combining the analytical model presented in Sommovigo et al. (2022) with recent observational constraints. Since an average stellar mass of $5 < z < 8$ galaxies is $M_{*} \sim 10^{10} M_{\odot}$, we calculate T_{dust} evolution with $M_{*} = 10^{10} M_{\odot}$. We start with Equations (7) and (9) in Sommovigo et al. (2022),

$$L_{\text{IR}} = \left(\frac{M_{\text{dust}}}{M_{\odot}} \right) \left(\frac{T_{\text{dust}}}{8.5 \text{ K}} \right)^{4+\beta_{\text{dust}}} \quad (9)$$

and

$$L_{\text{IR}} = (1 - e^{-\tau_{\text{eff}}}) L_{1500}^{\text{int}} = (1 - e^{-\tau_{\text{eff}}}) \mathcal{K}_{1500} \text{SFR}, \quad (10)$$

where Equation (9) can be obtained by integrating Equation (4) with ν . The dust mass can be calculated from the gas mass,

$M_{\text{dust}} = DM_{\text{gas}}$, where D represents the dust-to-gas ratio proportional to the metallicity $D = D_{\odot}(Z/Z_{\odot})$ as shown in Equation (3) in Sommovigo et al. (2022). Here \mathcal{K}_{1500} , L_{1500}^{int} , τ_{eff} and D_{\odot} are the conversion factor from the UV luminosity to the SFR ($=\text{SFR}/L_{1500}$), the intrinsic UV luminosity, the effective dust attenuation optical depth at 1500 Å and Galactic dust-to-gas ratio, respectively. A combination of these equations results in

$$T_{\text{dust}} = 8.5 \left[(1 - e^{-\tau_{\text{eff}}}) \frac{\mathcal{K}_{1500}}{D_{\odot}} \left(\frac{t_{\text{gas}}}{\text{yr}^{-1}} \cdot \frac{Z}{Z_{\odot}} \right)^{-1} \right]^{1/(4+\beta_{\text{dust}})}, \quad (11)$$

where t_{gas} represents the gas depletion timescale ($=M_{\text{gas}}/\text{SFR}$). Equation (11) corresponds to Equation (10) in Sommovigo et al. (2022). For the redshift evolution of the metallicity, we assume a power-law dependence of $d \log(\text{O}/\text{H})/dz = -0.11$ with a $z=0$ value of $12 + \log(\text{O}/\text{H}) = 8.77$ at $M_{*} = 10^{10} M_{\odot}$ (Sanders et al. 2021), which is consistent with recent JWST observations (Nakajima et al. 2023; Curti et al. 2024). As the metallicity dependence with redshift is still uncertain at $z > 5$ (Nakajima et al. 2023; Curti et al. 2024), we also compute the redshift evolution under the assumption of no metallicity evolution at $z > 3.3$. The gas depletion time decreases against the redshift as presented in Tacconi et al. (2020), $\log(t_{\text{dep}})[\text{Gyr}] = 0.19 - 0.98 \log(1+z)$ at $M_{*} = 10^{10} M_{\odot}$ on the main sequence (MS) ($\Delta\text{MS} = 0$). This discussion under the assumption of t_{gas} evolution is also presented in Sommovigo et al. (2022). We use $\mathcal{K}_{1500} = 1.4 \times 10^{10} L_{\odot}/(M_{\odot} \text{yr}^{-1})$ following in Tacconi et al. (2020) for the Chabrier IMF. Assuming $\beta_{\text{dust}} = 1.8$ and $D_{\odot} = 1/162$ (Rémy-Ruyer et al. 2014), Equation (11) becomes

$$T_{\text{dust}} = 19.55 \times [10^{0.11z}(1+z)^{0.98}(1 - e^{-\tau_{\text{eff}}})]^{1/5.8}. \quad (12)$$

Here we use $\tau_{\text{eff}} = 1.3$ to match the T_{dust} observation at $z = 0.5$, 27.2 K, in Schreiber et al. (2018) for galaxies with $M_{*} = 10^{9.5} - 10^{10} M_{\odot}$. The τ_{eff} value can be converted to $\text{IRX} = 0.56$ with

$$\text{IRX} = L_{\text{IR}}/L_{1500}^{\text{obs}} = (1 - e^{-\tau_{\text{eff}}})/e^{-\tau_{\text{eff}}} \quad (13)$$

based on Equation (10), which is consistent with the measurements up to $z \sim 6$ (Heinis et al. 2014; Whitaker et al. 2017; Fudamoto et al. 2020a; Algera et al. 2023). We plot the calculated T_{dust} evolution in Figure 10. The calculated T_{dust} matches our observational estimate for $z \sim 6-7$ galaxies ($T_{\text{dust}} = 40.9_{-9.1}^{+10.0}$ K).

The observed scatter of T_{dust} among $z \sim 6-7$ galaxies ($\Delta T_{\text{dust}} = 12$ K) can also be naturally explained by dispersions in the $M_{*}-Z$ and $M_{*}-\text{SFR}$ (so-called MS) relations. The dispersion from the MS of $\Delta\text{MS} = \pm 0.6$ dex (see Tacconi et al. 2020) results in the change of $\Delta T_{\text{dust}} \sim \pm 6$ K. A variance of $\Delta Z = \pm 0.3$ dex (see Sanders et al. 2021) from an average $M_{*}-Z$ relationship also changes T_{dust} by $\Delta T_{\text{dust}} \sim \pm 6$ K. Based on the fundamental mass-metallicity relation, the metallicity decreases with increasing SFR at the fixed stellar mass (e.g., Andrews & Martini 2013). Therefore, the positive offset from the MS may correlate with the negative offset in the average $M_{*}-Z$ relation, and both offsets result in the positive offset in T_{dust} . A sum of the dispersions in the MS and $M_{*}-Z$ relation is $\Delta T_{\text{dust}} = \pm 12$ K, which is comparable to our observational

result for the scatter in T_{dust} . We note that the assumption of β_{dust} (the Gaussian prior with $\langle \beta_{\text{dust}} \rangle = 1.8$ and $\sigma_{\beta_{\text{dust}}} = 0.5$) does not strongly contribute to the spread of T_{dust} given a small dispersion in the best-fit β_{dust} values of ~ 0.1 corresponding to $\Delta T_{\text{dust}} \sim 3$ K. The sampling of the continuum SED at longer wavelengths is necessary to obtain more precise β_{dust} values. Although our targeted galaxies do not have stellar mass M_{*} or the metallicity Z estimates due to the lack of rest-frame optical coverage, future JWST observations may be able to confirm what changes T_{dust} .

Interestingly, the high T_{dust} in the $z = 8.3$ MACS0416-Y1 (Tamura et al. 2019; Bakx et al. 2020) can also be explained by our calculation since its high sSFR (sSFR $\sim 2.0 \times 10^{-7} \text{Gyr}^{-1}$, corresponding to $\Delta\text{MS} \sim +1.5-1.6$ dex; Speagle et al. 2014; Topping et al. 2022) and low metallicity ($Z \sim 0.02-0.2Z_{\odot}$) are consistent with the measured lower limit of the dust temperature of $T_{\text{dust}} > 80$ K. Indeed, similar discussions about ΔT_{dust} have been presented in Sommovigo et al. (2022). They suggest ΔT_{dust} across the Universe can be explained by the variation in the metallicity with $0.1-1Z_{\odot}$ and the gas column density with $N_{\text{H}} \sim 0.03-0.5 \times 10^{21} \text{cm}^{-2}$. They also expect low metallicity ($Z \lesssim 0.3Z_{\odot}$) and high obscuration ($\tau_{\text{eff}} > 1$) can explain very hot dust in MACS0416-Y1. Please refer to Sommovigo et al. (2022) for more details on the models of the redshift evolution of T_{dust} and its scatter.

6. Summary and Conclusions

In this paper, we have examined the dust continuum emissions of 28 LBGs at $z \sim 5-8$ by utilizing multiband dust continuum observations obtained with ALMA. We conduct the MBB fitting with the MCMC algorithm to constrain parameters characterizing the FIR SEDs such as T_{dust} and M_{dust} . The 11 galaxies newly observed in our program, SERENADE, are originally UV-selected but cover a wide range of L_{IR} that spans from dust-poor galaxies (nondetection) to HyLIRG-class galaxies. The brightest galaxies in L_{IR} among our target galaxies exhibit intense starbursts comparable with the dusty star-forming galaxies at $z \sim 7$. From the individual measurements as well as the stacking analysis, we have found:

1. The $\text{IRX}-\beta_{\text{UV}}$ relation derived from multiband observations at $z \sim 6$ appears to be ~ 1 dex lower than that at $z \sim 3$ at $\beta_{\text{UV}} \sim 0$. Our observational constraints show good agreement with the previous $z \sim 5.5$ results based on single-band ALMA observations. The dust-obscured star formation calculated with the $M_{\text{UV}}-\beta_{\text{UV}}$ relation including fainter galaxies in literature and the $\text{IRX}-\beta_{\text{UV}}$ relations consistent with our results suggest $31_{-8}^{+8}\%$ contribution to the total SFRD at $z \sim 6$.
2. The $M_{\text{UV}}-f_{\text{obs}}$ relation at $z \sim 6$ is consistent with the results at $z \sim 5$ and $z \sim 7$. The contribution of dust-obscured star formation among LBGs based on the $M_{\text{UV}}-f_{\text{obs}}$ relation comprises $15_{-8}^{+17}\%$ of total SFRD, consistent with our estimates based on the $M_{\text{UV}}-\beta_{\text{UV}}$ and $\text{IRX}-\beta_{\text{UV}}$ relations within errors.
3. We present dust temperature measurements of LBGs at $z = 5-8$. Our T_{dust} measurements remain consistent with a linear redshift evolution $[\propto(1+z)^1]$. On the basis of the analytical model presented in Sommovigo et al. (2022), we calculate the average evolution of T_{dust} by combining t_{gas} (Tacconi et al. 2020) and Z evolution (Sanders et al. 2021) for galaxies with $M_{*} \sim 10^{10} M_{\odot}$ consistent with the

recent JWST measurements in Nakajima et al. (2023) and Curti et al. (2024). The calculated T_{dust} evolution exhibits an excellent agreement with our measurements at $z > 5$ as well as literature results at $z < 5$. The large observed scatter in T_{dust} can be interpreted as the results from the scatter around the star formation MS and the average mass–metallicity relation.

Since ALMA has capabilities of high-frequency observation in Bands 9/10, future ALMA high-frequency observations for a large sample of galaxies will further improve T_{dust} constraints and enable us to reach more precise conclusions. The recent JWST discovery of a large fraction of the broad-line AGN (Type 1) (Harikane et al. 2023b; Kocevski et al. 2023; Maiolino et al. 2023; Matthee et al. 2024) may suggest that the IR luminosity and the dust temperature are boosted by the possible presence of Type 2 AGN, as shown in (McKinney et al. 2021, see also Wiebe et al. 2009; Tsukui et al. 2023; Traina et al. 2024), although the estimated luminosity-weighted dust temperatures in this work have a very good agreement with those without strong effect of the AGN in the cosmological simulation (Di Mascia et al. 2021). Spatially resolved observations in Bands 9/10 may allow us to evaluate the AGN contribution to the radiation in the FIR wavelength. Also, future ALMA wideband sensitivity upgrades will enable us to access the very faint dust continuum from high- z galaxies to constrain the IRX or f_{obs} values of UV faint galaxies.

Acknowledgments

We thank the anonymous referee for constructive comments and suggestions. We thank L. Sommovigo, N. Kashikawa, Y. Sekimoto, M. Honma, T. Kodama, K. Nagamine, and K. Kohno for giving us helpful comments. This paper makes use of the following ALMA data: ADS/JAO.ALMA#2015.1.00540.S, #2015.1.01406.S, #2016.1.00954.S, #2017.1.00190.S, #2017.1.00508.S, #2017.1.00697.S, #2017.1.00775.S, #2019.1.01634.L, #2021.1.01297.S, #2021.1.00318.S, and #2022.1.00522.S. ALMA is a partnership of ESO (representing its member states), NSF (USA), and NINS (Japan), together with NRC (Canada), MOST and

ASIAA (Taiwan), and KASI (Republic of Korea), in cooperation with the Republic of Chile. The Joint ALMA Observatory is operated by ESO, AUI/NRAO, and NAOJ. IM is financially supported by Grants-in-Aid for Japan Society for the Promotion of Science (JSPS) Fellows (KAKENHI No. 22KJ0821). Y.H. is supported by JSPS KAKENHI grant No. 21K13953. H.U. acknowledges support from the JSPS KAKENHI grants (20H01953, 22KK0231). K.I. acknowledges support by grant PID2022-136828NB-C44 funded by MCIN/AEI/10.13039/501100011033. ANID—Millennium Science Initiative Program—ICN12_009 (F.E.B.), CATA-BASAL—FB210003 (F.E.B.), and FONDECYT Regular—1200495 (F.E.B.). Data analysis was in part carried out on the Multiwavelength Data Analysis System operated by the Astronomy Data Center (ADC), National Astronomical Observatory of Japan.

Appendix Flux Comparison

Because the amplitude of the visibilities at the zero baseline length could be a good indicator of the total flux, we also measure the fluxes from visibility data with UVMULTIFIT assuming the Sérsic index $n = 1$ just to check the flux recovery. Details of this visibility-based analysis will be presented in I. Mitsuhashi et al. (2024, in preparation).

In Figure 11, we compare the flux densities calculated with the different methodologies. Figure 11 (left) compares the fluxes derived from visibility fitting with UVMULTIFIT and from the image-based measurement. As described in Section 3, we apply two different ways to measure fluxes in the image, the CASA task IMFIT or peak flux with the tapered images. We find a very good consistency between visibility- and image-based flux densities we used in this work.

Figure 11 (right) plots the flux densities based on CASA/IMFIT against the peak flux in the images with different taper scales. The taper scale needed to recover total fluxes changes depending on the spatial extent of the sources. The uncertainties in the taper scales of $>2''$ tend to be larger than those from IMFIT although taper scales of $1''$ – $3''$ are necessary to recover the fluxes.

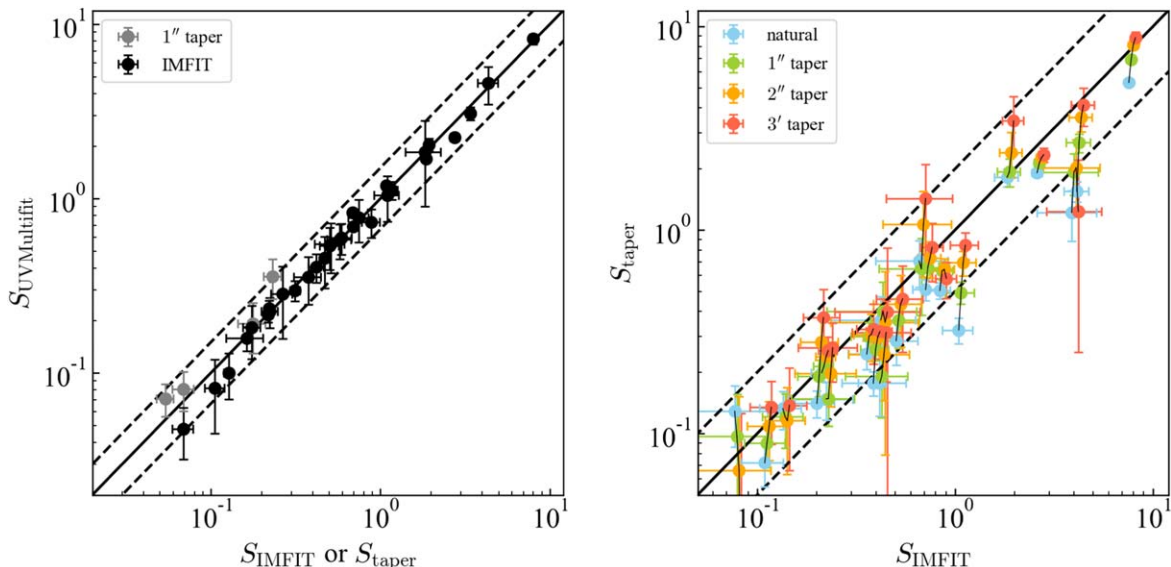



















Figure 11. Flux comparison between the different methodologies. (Left) Fluxes computed with visibility fitting vs. those with image-based IMFIT or peak fluxes. One-to-one relation and ± 0.3 dex are shown by the black solid and dashed lines. (Right) Fluxes computed from IMFIT and peak fluxes in the different taper scales of $0''$ (natural weighting), $1''$, $2''$, and $3''$. We again show one-to-one relation and ± 0.5 dex in black solid and dashed lines.

ORCID iDs

Ikki Mitsuhashi  <https://orcid.org/0000-0001-7300-9450>
 Yuichi Harikane  <https://orcid.org/0000-0002-6047-430X>
 Franz E. Bauer  <https://orcid.org/0000-0002-8686-8737>
 Tom J. L. C. Bakx  <https://orcid.org/0000-0002-5268-2221>
 Andrea Ferrara  <https://orcid.org/0000-0002-9400-7312>
 Seiji Fujimoto  <https://orcid.org/0000-0001-7201-5066>
 Takuya Hashimoto  <https://orcid.org/0000-0002-0898-4038>
 Akio K. Inoue  <https://orcid.org/0000-0002-7779-8677>
 Kazushi Iwasawa  <https://orcid.org/0000-0002-4923-3281>
 Yuri Nishimura  <https://orcid.org/0000-0003-0563-067X>
 Masatoshi Imanishi  <https://orcid.org/0000-0001-6186-8792>
 Yoshiaki Ono  <https://orcid.org/0000-0001-9011-7605>
 Yuma Sugahara  <https://orcid.org/0000-0001-6958-7856>
 Hideki Umehata  <https://orcid.org/0000-0003-1937-0573>
 Livia Vallini  <https://orcid.org/0000-0002-3258-3672>
 Tao Wang  <https://orcid.org/0000-0002-2504-2421>
 Jorge A. Zavala  <https://orcid.org/0000-0002-7051-1100>

References

- Aihara, H., AlSayyad, Y., Ando, M., et al. 2022, *PASJ*, 74, 247
 Aihara, H., Arimoto, N., Armstrong, R., et al. 2018, *PASJ*, 70, S4
 Akins, H. B., Fujimoto, S., Finlator, K., et al. 2022, *ApJ*, 934, 64
 Algera, H. S. B., Inami, H., Oesch, P. A., et al. 2023, *MNRAS*, 518, 6142
 Algera, H. S. B., Inami, H., Sommovigo, L., et al. 2024, *MNRAS*, 527, 6867
 Álvarez-Márquez, J., Burgarella, D., Buat, V., Ilbert, O., & Pérez-González, P. G. 2019, *A&A*, 630, A153
 Álvarez-Márquez, J., Burgarella, D., Heinis, S., et al. 2016, *A&A*, 587, A122
 Andrews, B. H., & Martini, P. 2013, *ApJ*, 765, 140
 Bakx, T. J. L. C., Sommovigo, L., Carniani, S., et al. 2021, *MNRAS*, 508, L58
 Bakx, T. J. L. C., Tamura, Y., Hashimoto, T., et al. 2020, *MNRAS*, 493, 4294
 Barisic, I., Faisst, A. L., Capak, P. L., et al. 2017, *ApJ*, 845, 41
 Barrufet, L., Oesch, P. A., Bouwens, R., et al. 2023a, *MNRAS*, 522, 3926
 Barrufet, L., Oesch, P. A., Weibel, A., et al. 2023b, *MNRAS*, 522, 449
 Béthermin, M., Daddi, E., Magdis, G., et al. 2015, *A&A*, 573, A113
 Béthermin, M., Fudamoto, Y., Ginolfi, M., et al. 2020, *A&A*, 643, A2
 Bouwens, R., Illingworth, G., Oesch, P., et al. 2023a, *MNRAS*, 523, 1009
 Bouwens, R. J., Illingworth, G. D., Franx, M., & Ford, H. 2007, *ApJ*, 670, 928
 Bouwens, R. J., Illingworth, G. D., Oesch, P. A., et al. 2012, *ApJ*, 754, 83
 Bouwens, R. J., Illingworth, G. D., Oesch, P. A., et al. 2014, *ApJ*, 793, 115
 Bouwens, R. J., Illingworth, G. D., Oesch, P. A., et al. 2015, *ApJ*, 803, 34
 Bouwens, R. J., Oesch, P. A., Stefanon, M., et al. 2021, *AJ*, 162, 47
 Bouwens, R. J., Smit, R., Schouws, S., et al. 2022, *ApJ*, 931, 160
 Bouwens, R. J., Stefanon, M., Brammer, G., et al. 2023b, *MNRAS*, 523, 1036
 Bowler, R. A. A., Dunlop, J. S., McLure, R. J., et al. 2014, *MNRAS*, 440, 2810
 Bowler, R. A. A., Inami, H., Sommovigo, L., et al. 2024, *MNRAS*, 527, 5808
 Bradley, L. D., Zitrin, A., Coe, D., et al. 2014, *ApJ*, 792, 76
 Calzetti, D., Armus, L., Bohlin, R. C., et al. 2000, *ApJ*, 533, 682
 Capak, P. L., Carilli, C., Jones, G., et al. 2015, *Natur*, 522, 455
 Casey, C. M. 2012, *MNRAS*, 425, 3094
 Casey, C. M., Zavala, J. A., Aravena, M., et al. 2019, *ApJ*, 887, 55
 Casey, C. M., Zavala, J. A., Manning, S. M., et al. 2021, *ApJ*, 923, 215
 Chabrier, G. 2003, *PASP*, 115, 763
 Charlot, S., & Fall, S. M. 2000, *ApJ*, 539, 718
 Chary, R., & Elbaz, D. 2001, *ApJ*, 556, 562
 Clements, D. L., Pearson, C., Farrah, D., et al. 2018, *MNRAS*, 475, 2097
 Coe, D., Zitrin, A., Carrasco, M., et al. 2013, *ApJ*, 762, 32
 Cortese, L., Fritz, J., Bianchi, S., et al. 2014, *MNRAS*, 440, 942
 Curti, M., Maiolino, R., Curtis-Lake, E., et al. 2024, *A&A*, 684, A75
 Curtis-Lake, E., McLure, R. J., Pearce, H. J., et al. 2012, *MNRAS*, 422, 1425
 da Cunha, E., Groves, B., Walter, F., et al. 2013, *ApJ*, 766, 13
 da Cunha, E., Hodge, J. A., Casey, C. M., et al. 2021, *ApJ*, 919, 30
 Di Mascia, F., Gallerani, S., Behrens, C., et al. 2021, *MNRAS*, 503, 2349
 Dudzevičiūtė, U., Smail, I., Swinbank, A. M., et al. 2020, *MNRAS*, 494, 3828
 Ellis, R. S., McLure, R. J., Dunlop, J. S., et al. 2013, *ApJL*, 763, L7
 Faisst, A. L., Capak, P. L., Yan, L., et al. 2017, *ApJ*, 847, 21
 Faisst, A. L., Fudamoto, Y., Oesch, P. A., et al. 2020a, *MNRAS*, 498, 4192
 Faisst, A. L., Schaerer, D., Lemaux, B. C., et al. 2020b, *ApJS*, 247, 61
 Ferrara, A., Hirashita, H., Ouchi, M., & Fujimoto, S. 2017, *MNRAS*, 471, 5018
 Ferrara, A., Sommovigo, L., Dayal, P., et al. 2022, *MNRAS*, 512, 58
 Finkelstein, S. L., Ryan, R. E., Jr., Papovich, C., et al. 2015, *ApJ*, 810, 71
 Fudamoto, Y., Oesch, P. A., Faisst, A., et al. 2020a, *A&A*, 643, A4
 Fudamoto, Y., Oesch, P. A., Magnelli, B., et al. 2020b, *MNRAS*, 491, 4724
 Fudamoto, Y., Oesch, P. A., Schouws, S., et al. 2021, *Natur*, 597, 489
 Fujimoto, S., Kohno, K., Ouchi, M., et al. 2023, arXiv:2303.01658
 Gordon, K. D., Clayton, G. C., Misselt, K. A., Landolt, A. U., & Wolff, M. J. 2003, *ApJ*, 594, 279
 Gruppioni, C., Béthermin, M., Loiacono, F., et al. 2020, *A&A*, 643, A8
 Harikane, Y., Laporte, N., Ellis, R. S., & Matsuoka, Y. 2020a, *ApJ*, 902, 117
 Harikane, Y., Nakajima, K., Ouchi, M., et al. 2024, *ApJ*, 960, 56
 Harikane, Y., Ono, Y., Ouchi, M., et al. 2022, *ApJS*, 259, 20
 Harikane, Y., Ouchi, M., Inoue, A. K., et al. 2020b, *ApJ*, 896, 93
 Harikane, Y., Ouchi, M., Oguri, M., et al. 2023a, *ApJS*, 265, 5
 Harikane, Y., Zhang, Y., Nakajima, K., et al. 2023b, *ApJ*, 959, 39
 Hashimoto, T., Inoue, A. K., Mawatari, K., et al. 2019, *PASJ*, 71, 71
 Heinis, S., Buat, V., Béthermin, M., et al. 2014, *MNRAS*, 437, 1268
 Huang, K.-H., Bradač, M., Lemaux, B. C., et al. 2016, *ApJ*, 817, 11
 Inami, H., Algera, H. S. B., Schouws, S., et al. 2022, *MNRAS*, 515, 3126
 Inoue, A. K., Hashimoto, T., Chihara, H., & Koike, C. 2020, *MNRAS*, 495, 1577
 Jarvis, M. J., Bonfield, D. G., Bruce, V. A., et al. 2013, *MNRAS*, 428, 1281
 Khusanova, Y., Béthermin, M., Le Fèvre, O., et al. 2021, *A&A*, 649, A152
 Knudsen, K. K., Watson, D., Frayer, D., et al. 2017, *MNRAS*, 466, 138
 Kocevski, D. D., Onoue, M., Inayoshi, K., et al. 2023, *ApJL*, 954, L4
 Lamperti, I., Saintonge, A., De Looze, I., et al. 2019, *MNRAS*, 489, 4389
 Laporte, N., Katz, H., Ellis, R. S., et al. 2019, *MNRAS*, 487, L81
 Lawrence, A., Warren, S. J., Almaini, O., et al. 2007, *MNRAS*, 379, 1599
 Le Fèvre, O., Béthermin, M., Faisst, A., et al. 2020, *A&A*, 643, A1
 Lee, K.-S., Dey, A., Reddy, N., et al. 2011, *ApJ*, 733, 99
 Liang, L., Feldmann, R., Kereš, D., et al. 2019, *MNRAS*, 489, 1397
 Lilly, S. J., Le Fèvre, O., Hammer, F., & Crampton, D. 1996, *ApJL*, 460, L1
 Looser, T. J., D'Eugenio, F., Maiolino, R., et al. 2024, *Natur*, 629, 53
 Ma, X., Hayward, C. C., Casey, C. M., et al. 2019, *MNRAS*, 487, 1844
 Madau, P., & Dickinson, M. 2014, *ARA&A*, 52, 415
 Madau, P., Ferguson, H. C., Dickinson, M. E., et al. 1996, *MNRAS*, 283, 1388
 Magnelli, B., Elbaz, D., Chary, R. R., et al. 2009, *A&A*, 496, 57
 Magnelli, B., Elbaz, D., Chary, R. R., et al. 2011, *A&A*, 528, A35
 Magnelli, B., Lutz, D., Saintonge, A., et al. 2014, *A&A*, 561, A86
 Magnelli, B., Popesso, P., Berta, S., et al. 2013, *A&A*, 553, A132
 Maiolino, R., Zitrin, A., Stark, D. P., et al. 2018, *MNRAS*, 479, 1180
 Maiolino, R., Scholtz, J., Curtis-Lake, E., et al. 2023, arXiv:2308.01230
 Mallery, R. P., Mobasher, B., Capak, P., et al. 2012, *ApJ*, 760, 128
 Marrone, D. P., Spilker, J. S., Hayward, C. C., et al. 2018, *Natur*, 553, 51
 Matsuoka, Y., Iwasawa, K., Onoue, M., et al. 2018a, *ApJS*, 237, 5
 Matsuoka, Y., Iwasawa, K., Onoue, M., et al. 2019, *ApJ*, 883, 183
 Matsuoka, Y., Onoue, M., Kashikawa, N., et al. 2016, *ApJ*, 828, 26
 Matsuoka, Y., Onoue, M., Kashikawa, N., et al. 2018b, *PASJ*, 70, S35
 Matthee, J., Naidu, R. P., Brammer, G., et al. 2024, *ApJ*, 963, 129
 McKinney, J., Hayward, C. C., Rosenthal, L. J., et al. 2021, *ApJ*, 921, 55
 Mehta, V., Scarlata, C., Capak, P., et al. 2018, *ApJS*, 235, 36
 Meurer, G. R., Heckman, T. M., & Calzetti, D. 1999, *ApJ*, 521, 64
 Moutard, T., Sawicki, M., Arnouts, S., et al. 2020, *MNRAS*, 494, 1894
 Nakajima, K., Ouchi, M., Isobe, Y., et al. 2023, *ApJS*, 269, 33
 Oesch, P. A., Bouwens, R. J., Carollo, C. M., et al. 2010, *ApJL*, 725, L150
 Oesch, P. A., Bouwens, R. J., Illingworth, G. D., et al. 2013, *ApJ*, 773, 75
 Ono, Y., Ouchi, M., Harikane, Y., et al. 2018, *PASJ*, 70, S10
 Overzier, R. A., Heckman, T. M., Wang, J., et al. 2011, *ApJL*, 726, L7
 Pettini, M., Kellogg, M., Steidel, C. C., et al. 1998, *ApJ*, 508, 539
 Pierre, M., Valtchanov, I., Altieri, B., et al. 2004, *JCAP*, 2004, 011
 Planck Collaboration, Abergel, A., Ade, P. A. R., et al. 2014, *A&A*, 571, A11
 Prevot, M. L., Lequeux, J., Maurice, E., Prevot, L., & Rocca-Volmerange, B. 1984, *A&A*, 132, 389
 Reddy, N. A., Erb, D. K., Pettini, M., Steidel, C. C., & Shapley, A. E. 2010, *ApJ*, 712, 1070
 Reddy, N. A., Kriek, M., Shapley, A. E., et al. 2015, *ApJ*, 806, 259
 Reddy, N. A., Oesch, P. A., Bouwens, R. J., et al. 2018, *ApJ*, 853, 56
 Rémy-Ruyer, A., Madden, S. C., Galliano, F., et al. 2014, *A&A*, 563, A31
 Reuter, C., Vieira, J. D., Spilker, J. S., et al. 2020, *ApJ*, 902, 78
 Riechers, D. A., Bradford, C. M., Clements, D. L., et al. 2013, *Natur*, 496, 329
 Robertson, B. E., Ellis, R. S., Dunlop, J. S., McLure, R. J., & Stark, D. P. 2010, *Natur*, 468, 49
 Sanders, R. L., Shapley, A. E., Jones, T., et al. 2021, *ApJ*, 914, 19
 Sawicki, M. 2012, *PASP*, 124, 1208
 Schouws, S., Stefanon, M., Bouwens, R., et al. 2022, *ApJ*, 928, 31
 Schreiber, C., Elbaz, D., Pannella, M., et al. 2018, *A&A*, 609, A30
 Scoville, N., Aussel, H., Brusa, M., et al. 2007, *ApJS*, 172, 1

- Smit, R., Bouwens, R. J., Carniani, S., et al. 2018, *Natur*, **553**, 178
- Sommovigo, L., Ferrara, A., Carniani, S., et al. 2021, *MNRAS*, **503**, 4878
- Sommovigo, L., Ferrara, A., Pallottini, A., et al. 2020, *MNRAS*, **497**, 956
- Sommovigo, L., Ferrara, A., Pallottini, A., et al. 2022, *MNRAS*, **513**, 3122
- Song, M., Finkelstein, S. L., Ashby, M. L. N., et al. 2016, *ApJ*, **825**, 5
- Speagle, J. S., Steinhardt, C. L., Capak, P. L., & Silverman, J. D. 2014, *ApJS*, **214**, 15
- Steidel, C. C., Adelberger, K. L., Giavalisco, M., Dickinson, M., & Pettini, M. 1999, *ApJ*, **519**, 1
- Stiavelli, M., Morishita, T., Chiaberge, M., et al. 2023, *ApJL*, **957**, L18
- Sugahara, Y., Inoue, A. K., Hashimoto, T., et al. 2021, *ApJ*, **923**, 5
- Tacchella, S., Finkelstein, S. L., Bagley, M., et al. 2022, *ApJ*, **927**, 170
- Tacconi, L. J., Genzel, R., & Sternberg, A. 2020, *ARA&A*, **58**, 157
- Takeuchi, T. T., Yuan, F.-T., Ikeyama, A., Murata, K. L., & Inoue, A. K. 2012, *ApJ*, **755**, 144
- Tamura, Y., Mawatari, K., Hashimoto, T., et al. 2019, *ApJ*, **874**, 27
- Topping, M. W., Stark, D. P., Endsley, R., et al. 2022, *MNRAS*, **516**, 975
- Traina, A., Gruppioni, C., Delvecchio, I., et al. 2024, *A&A*, **681**, A118
- Tsukui, T., Wisnioski, E., Krumholz, M. R., & Battisti, A. 2023, *MNRAS*, **523**, 4654
- Vallini, L., Witstok, J., Sommovigo, L., et al. 2024, *MNRAS*, **527**, 10
- Viero, M. P., Sun, G., Chung, D. T., Monceli, L., & Condon, S. S. 2022, *MNRAS*, **516**, L30
- Wang, T., Schreiber, C., Elbaz, D., et al. 2019, *Natur*, **572**, 211
- Watson, D., Christensen, L., Knudsen, K. K., et al. 2015, *Natur*, **519**, 327
- Weaver, J. R., Kauffmann, O. B., Ilbert, O., et al. 2022, *ApJS*, **258**, 11
- Whitaker, K. E., Pope, A., Cybulski, R., et al. 2017, *ApJ*, **850**, 208
- Wiebe, D. V., Ade, P. A. R., Bock, J. J., et al. 2009, *ApJ*, **707**, 1809
- Willott, C. J., Carilli, C. L., Wagg, J., & Wang, R. 2015, *ApJ*, **807**, 180
- Witstok, J., Jones, G. C., Maiolino, R., Smit, R., & Schneider, R. 2023, *MNRAS*, **523**, 3119
- Witstok, J., Smit, R., Maiolino, R., et al. 2022, *MNRAS*, **515**, 1751
- Wong, Y. H. V., Wang, P., Hashimoto, T., et al. 2022, *ApJ*, **929**, 161
- Yamanaka, S., & Yamada, T. 2019, *PASJ*, **71**, 51
- Zavala, J. A., Casey, C. M., Manning, S. M., et al. 2021, *ApJ*, **909**, 165
- Zavala, J. A., Montaña, A., Hughes, D. H., et al. 2018, *NatAs*, **2**, 56